

Influence of pore fluid on grain-scale interactions and mobility of granular flows of differing volume

Alexander M. Taylor-Noonan¹, Elisabeth T. Bowman², Brian W. McArdell³, Roland Kaitna⁴, Jim N. McElwaine⁵, W. Andy Take⁶

¹Ph.D. Graduate, Department of Civil Engineering, Queen's University at Kingston, Canada (ORCID 0000-0002-5590-7350)

²Reader, Department of Civil Engineering, University of Sheffield, United Kingdom (ORCID 0000-0001-7868-6688)

³Geologist, Swiss Federal Institute for Forest, Snow and Landscape Research (WSL), Switzerland (ORCID 0000-0002-5322-8741)

⁴Associate Professor, Institute of Mountain Risk Engineering (IAN-BOKU), University of Natural Resources and Life Sciences, Vienna, Austria (ORCID 0000-0002-2289-723X)

⁵Professor of Geohazards, Department of Earth Sciences, Durham University, United Kingdom (ORCID 0000-0002-6292-2014)

⁶Professor & Canada Research Chair in Geotechnical Engineering, Department of Civil Engineering, Queen's University at Kingston, Canada (ORCID 0000-0002-8634-1919)

Key Points:

- Dry granular flows of five volumes between 0.2 to 1.0 m³ observed to yield a constant travel angle in flume tests
- Saturated flows of the same granular material exhibited a nonlinear decrease in travel angle with increasing volume
- Results provide unique test scenario for simulations by constraining friction properties prior to exploring pore fluid effects

Abstract

The presence of a pore fluid is recognized to significantly increase the mobility of saturated over dry granular flows. However, experimental studies in which both the bulk-scale (runout) and grain-scale behaviour of identical granular material in a dry and saturated initial state are directly compared are rare. Further, the mechanisms through which pore fluid increases mobility may not be captured in experimental flows of small volume typical of laboratory conditions. Here we present the results of dry and initially fluid saturated or “wet” experimental flows in a large laboratory flume for five source volumes of 0.2 to 1.0 m³. Our results demonstrate that the striking differences in the nature of interactions at the particle scale between wet and dry flows can be directly linked to macro-scale behaviour: in particular, a greatly increased mobility for wet granular flows compared to dry, and a significant influence of scale as controlled by source volume. This dataset provides valuable test scenarios to explore the fundamental mechanisms through which the presence of a pore fluid increases flow mobility by first constraining the frictional properties of the material (dry experiments), permitting an independent evaluation of the implementation of interstitial fluid effects in numerical runout models (wet experiments).

Plain Language Summary

An accurate prediction of how fast and how far a landslide, such as a debris flow, will travel is essential to define the hazard posed to life and property by these geophysical flows. While dry frictional flows often behave according to the simple physics of friction resisting motion, water saturated granular flows tend to travel farther and faster than the same scenario under dry conditions. In this paper we explore this phenomenon in detail, using high-speed video analysis to look for and quantify differences in grain-scale behaviour that might lead to increased mobility in saturated over dry flows, and high definition laser scans to quantify how far the debris travelled. Large flume tests comparing dry versus saturated flows for five source volumes of 0.2 to 1.0 cubic metres reveal that, in contrast to dry flows, saturated flows travel significantly farther as the volume of the landslide increases. This data is unique as it will enable researchers to test how well numerical simulations are able to model the travel behaviour of the same material in a dry and water saturated state.

1 Introduction

The quantification of the hazard posed by a potential landslide source volume requires an accurate prediction of the travel path and distal reach of the debris. This is generally accomplished in practice by using runout observations from past landslide events in the same location or similar geologic materials to delineate potential hazard areas for future landslides. These observations are then used either within an empirical-statistical approach to define runout exceedance probability (Legros, 2002) or by inferring debris rheological models and parameters from numerical simulations to match runout and inundation depth trimlines of historical events (McDougall, 2017). Heim’s Ratio (H/L) was an early empirical-statistical proposal of a parameter for risk assessment by geometrical similarity (Figure 1). The total runout length L has the components of translation of the centre of mass L_{COM} and spreading of the material ahead of the centre-of-mass S_f (Dade & Huppert, 1998; Staron & Lajeunesse, 2009), while the difference in elevation, H , is measured from the back of the head scarp to the front of the debris. The total runout length L is typically of greatest interest for hazard assessment whereas the potential energy of the source volume is often equated to H . As a further development to Heim’s Ratio, Perez & Aharonov (2015) then presented a functional model in which the contribution of spreading of the material is related to channel geometry as well as the surface angle of the final deposit.

The travel angle $\alpha_g = \arctan(H_{COM}/L_{COM})$ is defined as the angle of inclination between the centre of mass of the runout deposit and the centre of mass of the source vol-

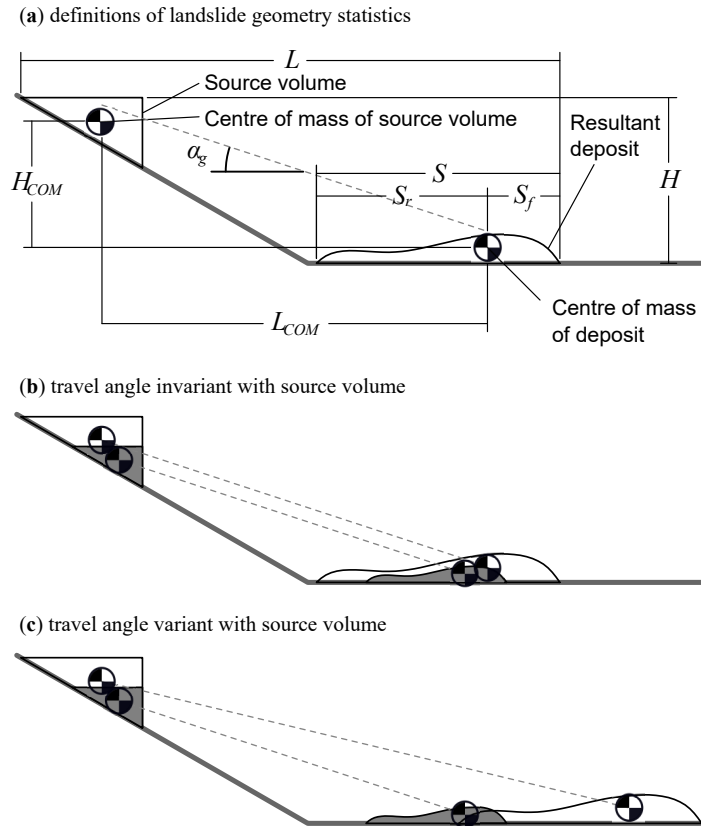


Figure 1. Schematic illustration of flows in a simple planar flume, showing (a) definition of geometry statistics, (b) the case where the travel angle α_g is invariant with source volume, and (c) potential variation of α_g with changing source volume indicating a variation within the rheology.

76 ume and has been associated with an apparent friction coefficient (e.g. Parez & Aharonov,
 77 2015). Conceptually, the travel angle may be invariant with source volume (Figure 1b),
 78 or it may vary with the source volume (Figure 1c) where scale effects are significant. Ag-
 79 gregated observations of historical debris flows, compiled by Corominas (1996) and Rick-
 80 enmann (2011), illustrate the general trend of decreasing travel angle (signifying increased
 81 mobility and a decrease in effective flow resistance) as source volume increases. While
 82 there is a lack of consensus in the literature, collisionality (e.g. Armanini 2013), fragmen-
 83 tation (e.g. Bowman et al. 2012; Caballero et al. 2014), pore pressure diffusion length-
 84 scales (e.g. Iverson 2015; Kaitna et al. 2016), and thermal effects (e.g. Voight & Faust
 85 1982; Goren & Aharonov 2007; Alonso et al. 2016; Fischer et al. 2018) amongst other
 86 hypotheses (e.g. effects at the laboratory scale such as side wall effects and air drag; Bryant
 87 et al. 2015; Kessler et al. 2020) have been investigated as potential mechanisms through
 88 which larger volume landslides achieve higher mobility.

89 Experimental flume flows using dry granular material have shown that when the rheol-
 90 ogy of the flow is very simple, the runout behavior can be straightforwardly related to
 91 general physical parameters like slope angle, basal friction and grain size (e.g. Mangeney
 92 et al. 2010) or predicted using depth-averaged models (e.g. Bryant et al. 2015). Flows
 93 on fully saturated or initially saturated materials have shown rheological changes with
 94 source volume (e.g. de Haas et al. 2015), fines content or moisture content (e.g. Kaitna
 95 et al. 2014; Hürlimann et al. 2015; Zhou et al. 2018).

96 Numerical simulations of landslide runout offer the ability to release a source volume,
 97 propagate its flow over a 2D or 3D geometrical representation of the terrain, and pro-
 98 vide estimates of inundation depth, velocity, and definition of the maximum distal reach
 99 of the debris for a given pairing of a resistance law and respective model parameter(s).
 100 In the case the moving mass is modelled based on an equivalent fluid concept (Hung, 1995),
 101 the resistance law is chosen based on the nature of the flow. That can range from
 102 a granular flow to a fully liquefied flow for which the effect of pore fluid is of major im-
 103 portance.

104 For granular flows, the main source of flow resistance stems from particle friction and
 105 particle collisions. In dense granular flows, particle contacts are long-lasting and force
 106 chains develop. For natural flows in a frictional regime, the recently developed $\mu(I)$ rhe-
 107 ology may be appropriate (Forterre & Pouliquen, 2008). A collisional regime can occur
 108 when the concentration of solids, represented by the volume fraction ν as the portion of
 109 total volume occupied by solid particles, is too low to maintain these long-lasting con-
 110 tacts (Bagnold, 1954; Jenkins & Savage, 1983). In a collisional regime the flow resistance
 111 comes not from friction but instead a collisional viscosity dependent on ν and the rate
 112 of collisions (e.g. Lun & Savage, 1986). The transition between the idealized regimes is
 113 not abrupt and the regimes are thought to exist simultaneously in the transition (An-
 114 cey & Evesque, 2000; Armanini, 2013). The interstitial fluid would also affect this collisional-
 115 frictional network of discrete particles.

116 With the addition of an interstitial fluid to a granular flow, particles are subject to both
 117 buoyancy and drag forces (Armanini, 2013; Iverson, 1997). Particle buoyancy reduces
 118 the interparticle stresses, which is represented on a macro scale by the concept of geotech-
 119 nical effective stress $\sigma' = \sigma - u$, where σ is total stress, u is pore pressure. In a fric-
 120 tional continuum material, the shear resistance from friction is proportional to the ef-
 121 fective stress (e.g. $\tau = \sigma' \tan \phi'$) - i.e. the Mohr-Coulomb criterion.

122 For a fully liquefied or low solids content flow, the effect of interstitial fluid may be more
 123 conveniently modelled by a non-Newtonian phenomenological flow law (Ancey, 2007),
 124 which is characterized by a distinct velocity profile. In both cases, pore pressure effects
 125 are typically considered to be constant during the duration of the flow. The validity of
 126 this assumption has been explored in Tayyebi et al. (2021), who suggest model choice
 127 should be guided through a consideration of two competing characteristic times: i) con-
 128 solidation time and ii) propagation time. For scenarios in which the time of pore pres-
 129 sure dissipation is rapid in comparison to the travel time, the high permeability debris

130 is unlikely to retain excess positive pore pressure (e.g. Iverson 2015; Pudasaini et al. 2005;
131 Pastor et al. 2014; Kaitna et al. 2016), permitting simpler models of pore pressure ef-
132 fects to be used. On the other hand, it may be appropriate for fully undrained models
133 to simulate lower permeability flows, such as high water content slurries or liquefied de-
134 bris. Debris flows with intermediate permeability between these two end members have
135 the most computationally complex requirements for numerical simulation as the consol-
136 idation time and travel time can be of the same order.

137 Recent observations of large landslide events which include a transition from a granu-
138 lar flow to a liquefied flow (e.g. Walter et al., 2020; Shugar et al., 2021) and progress in
139 monitoring of debris flows, including basal stresses (e.g. McArdell et al., 2007) and ve-
140 locity profiles (Nagl et al., 2020) highlight the importance of the fluid in granular flows.

141 The addition of an interstitial fluid is therefore recognized to have a dominant impact
142 on the mobility of the flow. Impulse releases of an opaque material from behind a rapidly
143 opening gate have been performed by the USGS (e.g. Iverson et al. 2010) on a large scale
144 with a laterally unconfined runout area or at laboratory scale (e.g. Hürlimann et al. 2015).
145 Flows may also be triggered by moving water (e.g. Tsubaki et al. 1983; Hotta 2012; Lan-
146 zoni et al. 2017). A recirculating flume was used by Armanini et al. (2005) to host a long-
147 duration debris flow from which grain-scale measurements of volume fraction and veloc-
148 ity could be taken.

149 However, experimental studies in which both the bulk-scale (runout) and grain-scale be-
150 haviour of identical granular material in a dry and saturated initial state are directly com-
151 pared are rare. The comparison would provide a unique opportunity to test numerical
152 simulation outcomes by first constraining the frictional properties of the material (i.e.
153 matching the runout behaviour of the dry experiments of different source volumes) be-
154 fore independently evaluating the implementation of rheological models to account for
155 buoyancy, fluid drag, and pore pressure affecting the frictional material. The relative con-
156 tributions of each mechanism may be revealed by matching the volume scaling effects.

157 We performed a series of experiments on the end member cases of high permeability de-
158 bris which is initially dry or initially saturated with the objective of defining the influ-
159 ence of interstitial fluid and landslide volume on the runout distance and the relative con-
160 tributions of translation and spreading in a material in which excess pore pressure is not
161 expected to occur. A monodisperse material was used to ensure no segregation of par-
162 ticle size would take place during flow which could alter the rheologic behaviour, other
163 than that caused by variation in solid and fluid concentration. Granular material was
164 selected of a large enough grain size to isolate the effects of buoyancy and drag on the
165 flows and allow for particle-level observation of contact behaviour and flow regimes. Each
166 flow was initiated from a well-defined state and observed comprehensively during the travel
167 and arrest phases. Dry flows of the identical source volumes were also tested as a direct
168 point of reference for comparison.

169 In the remainder of the manuscript, we first describe the research flume, instrumenta-
170 tion, and high-speed video analysis methods used for the experiments. The flow regimes
171 of both dry and initially saturated 0.8 m^3 flows are then described and illustrated us-
172 ing representative frames and depth profiles. Next, velocity and volume fraction results
173 are presented for volumes ranging between 0.2 to 1.0 m^3 to illustrate the variation in regimes.
174 Finally, laser scanning results of the deposit morphology of each trial are used to explore
175 the nature of the relationship between travel angle and source volume for both dry and
176 wet flows.

177 2 Experimental Setup & Methodology

178 The experiments consisted of a series of granular flows in a large indoor testing facility
179 (Figure 2). The 2.09 m wide flume features a 8.23 m long section inclined 30° from hor-
180 izontal and a 33 m long horizontal runout section. For the entirety of the inclined por-

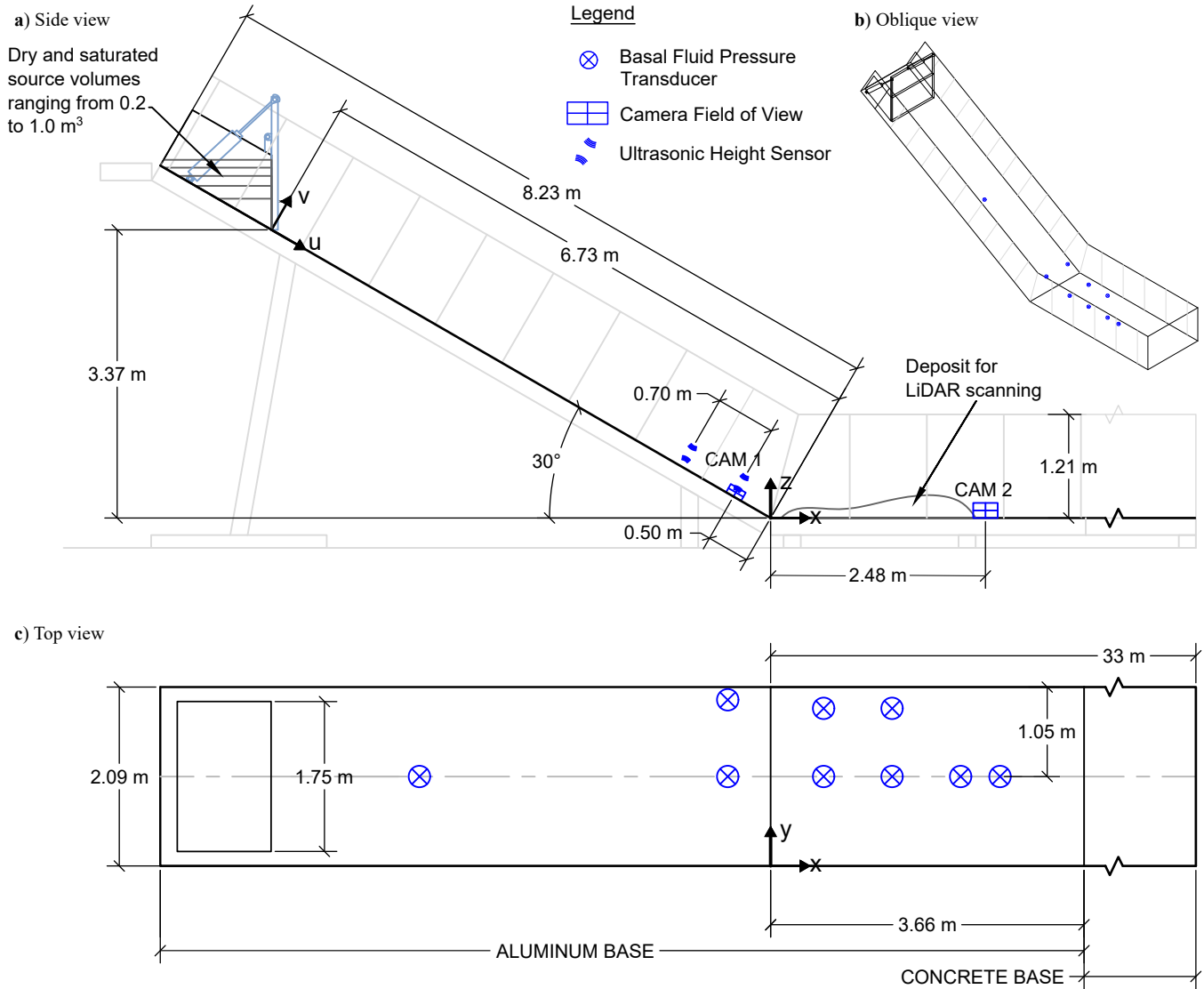


Figure 2. Diagram of (a) side profile, (b) oblique view, (c) top view of the experimental flume, illustrating the locations of high-speed video camera fields of view, basal fluid pressure transducers, and ultrasonic height sensors.

181 tion and for the first 3.68 m of the horizontal runout section, the base of the flume is con-
182 structed from bare aluminum and the side walls of the flume are glass to permit obser-
183 vation of the flows. Further down the flume, the base is constructed from smooth con-
184 crete. At the top, a release box with a hinged door can accommodate over 1.0 m³ of sat-
185 urated material. The door was rapidly opened using pneumatic cylinders to initiate the
186 experiment, with the door moving clear of the material within 0.4 s. At the completion
187 of the test, the final deposit shape was surveyed using a Faro Focus S 150 Light Detec-
188 tion and Ranging (LiDAR) scanner from two or more scanning positions.

189 2.1 Video Capture & Instrumentation

190 During the test, a Phantom v2512 high-speed video camera was located near the end of
191 the inclined portion of the flume (indicated as ‘CAM1’ on Figure 2) to capture mature
192 flow behaviour in the travel stage. The camera was oriented in a side-on configuration
193 to observe through the transparent glass side walls, rotated such that the width of the
194 image was parallel to the base of the flume. The camera was set to capture a 1280 x 800
195 pixel greyscale image at a frame rate of 7,500 - 10,000 fps (frames per second). A Tok-
196 ina 100 mm f/2.8 Macro lens was used at its widest aperture to limit the depth of field
197 and distinguish only the particles next to the glass side walls. The field of view was ap-
198 proximately 220 mm by 136 mm. A typical particle of 3.85 mm diameter was represented
199 by a 23 pixel width in the resulting image.

200 As only one high-speed video camera was available, two initially saturated flows (0.4 and
201 0.8 m³ source volumes) were repeated with the same camera and lens situated within
202 the horizontal portion of the flume (‘CAM2’ on Figure 2). At this location, the camera
203 was situated further back from the sidewall. The field of view was approximately 285
204 by 178 mm, with a typical particle represented by 17 pixels.

205 Nine fluid pressure transducer sensors were installed into the base of the flume to quan-
206 tify the basal fluid pressure (Figure 2). The sensors (TE Connectivity model U5244-000002-
207 14BG, 0 to 140 mbar range, manufacturer’s stated accuracy 7 mm, total error band 18
208 mm) were threaded directly into the flume. The fluid could enter each sensor through
209 seven holes of 2 mm diameter.

210 Two ultrasonic distance sensors (model S18UUAQ, Banner Engineering Corp., 2.5 ms
211 response time) were mounted above the inclined section of the flume, along the flume
212 centreline (Figure 2). These sensors recorded the flow height away from the influence of
213 the glass sidewalls by measuring the distance between the sensor and the top of the flow,
214 normal to the flume base.

215 The sensor signals were sampled and recorded at 2000 Hz. During the experiments, the
216 pressure sensors were subject to noise considered to be resonance of the flume. The nat-
217 ural frequency of the flume structure was measured at approximately 140 Hz. To coun-
218 teract this noise, the pressure sensor output signals were filtered using a 80 Hz low-pass
219 Butterworth filter.

220 2.2 Materials and Preparation

221 Pseudo-spherical ceramic beads, manufactured by Saint-Gobain Norpro and marketed
222 as Denstone 2000 Support Media, were used as the granular material for the experiments.
223 These beads were chosen for their pseudospherical shape, relatively uniform diameter,
224 and ability to be reused for multiple trials with minimal breakdown. The physical prop-
225 erties of a representative sample of 30 beads were measured and tabulated by Coombs
226 et al. (2019). The beads were found to have an average diameter of 3.85 mm, grain spheric-
227 ity of approximately 95%, and grain density of 2241 kg m⁻³. The bulk density was mea-
228 sured by Coombs (2018) as 1400 kg m⁻³, corresponding to a volume fraction of $\nu = 0.63$.
229 According to the manufacturer, the hardness of the beads exceeds 6.5 on the Mohs scale.
230 Triaxial tests conducted by Raymond (2002) gave effective friction angles of 33.7° at 20 kPa
231 confining pressure.

232 The source volumes tested were comprised of 0.2, 0.4, 0.6, 0.8, and 1.0 m³. In each of
 233 the dry and initially saturated states, the material was made level in the release box us-
 234 ing a rake. In the initially saturated state, the pore spaces were inundated with water
 235 but ponding water on top of the beads was minimized.

236 3 High-speed video analysis and calculated quantities

237 High-speed video was used to observe the flow structure and to provide images for fur-
 238 ther analysis. In this section, we discuss the image analysis methods used to identify the
 239 velocity and volume fraction for each test.

240 3.1 Particle displacement and velocity

241 The Particle Tracking Velocimetry (PTV) method involves first identifying the particle
 242 locations in selected frames and then using a PTV algorithm to link individual particles
 243 in successive frames (Brevis et al., 2010; Gollin et al., 2017; Taylor-Noonan et al., 2021).
 244 In our experiments, the camera is oriented to match the inclination of the flume base to
 245 optimise the field of view, e.g. so the particle movement vectors (Figure 3a) are gener-
 246 ally horizontal in the illustrations. The direction of gravity is noted on the figure.

247 The images were analyzed in sets of fifty (50) images. Each set was initiated at an in-
 248 terval of $t = 0.05$ s during the passage of the flow. Within each set, the frames were
 249 selected from the 7,500 - 10,000 fps video such that the analysed frames were $\Delta t = .0004$ s
 250 apart (equivalent to 2,500 fps). For a particle moving at 5 metres per second, the move-
 251 ment was 11.5 pixels and the resulting ratio of particle movement per frame to particle
 252 diameter was 0.52. For a particle moving at 1 metre per second, the corresponding move-
 253 ment was 2.3 pixels. The results were grouped into bins (shown by red lines on Figure 3)
 254 to prepare depth profiles of the quantities, each drawn parallel to the flume base with
 255 height equal to one average particle diameter. Each vector was decomposed into com-
 256 ponents parallel (streamwise) and perpendicular to the flume base.

257 Velocity profiles (Figure 3b) were calculated by averaging the components of each vec-
 258 tor located within the bin, for all pairs of frames that comprise the set. From the pro-
 259 file of streamwise velocity u , the shear strain rate with respect to depth is defined here
 260 by $\dot{\gamma} \equiv \partial u / \partial z$. This quantity indicates relative displacement within the flow. The ve-
 261 locity of the lowest bin, adjacent to the flume base, was considered to be the basal slip
 262 velocity. As an example, Figure 4 presents the free surface and basal slip velocities for
 263 representative 0.8 m³ dry and wet flows.

264 3.2 Volume Fraction

265 The volume fraction ν forms the basis for classification in Kinetic Theory and Extended
 266 Kinetic Theory (e.g. Lun, 1991; Jenkins, 2007; Chialvo et al., 2012). Randomly close packed
 267 spheres correspond to $\nu_{rcp} \approx 0.64$ (Allen & Thomas, 1999). Various contributors to EKT
 268 propose the frictional regime begins between $0.583 \leq \nu \leq 0.613$ when long-lasting par-
 269 ticle contacts develop. Jenkins (2007) further divided the collisional regime at $\nu = 0.49$
 270 into a ‘dense collisional’ and ‘dilute collisional’ regime based on a change in the likeli-
 271 hood of a particle collision. This proposed classification has been shown in the background
 272 of volume fraction plots in the following sections.

273 Here, ν was estimated using the method proposed by Capart et al. (2002), which con-
 274 siders the size and shape of Voronoï polygons drawn around the identified particle lo-
 275 cations as the basis of estimation. The image plane is divided into regions, each contain-
 276 ing one identified particle centroid location (Figure 3c). The regions are drawn such that
 277 all points in the region are closer to that identified particle than any other.

278 This method uses a roundness parameter $\xi = 4\pi A / P^2$ where A and P are the area and
 279 perimeter of the Voronoï polygon around the particle, respectively. The roundness pa-
 280 rameter ξ is calculated for all the particles in a bin over all the frames in each set. Voronoï

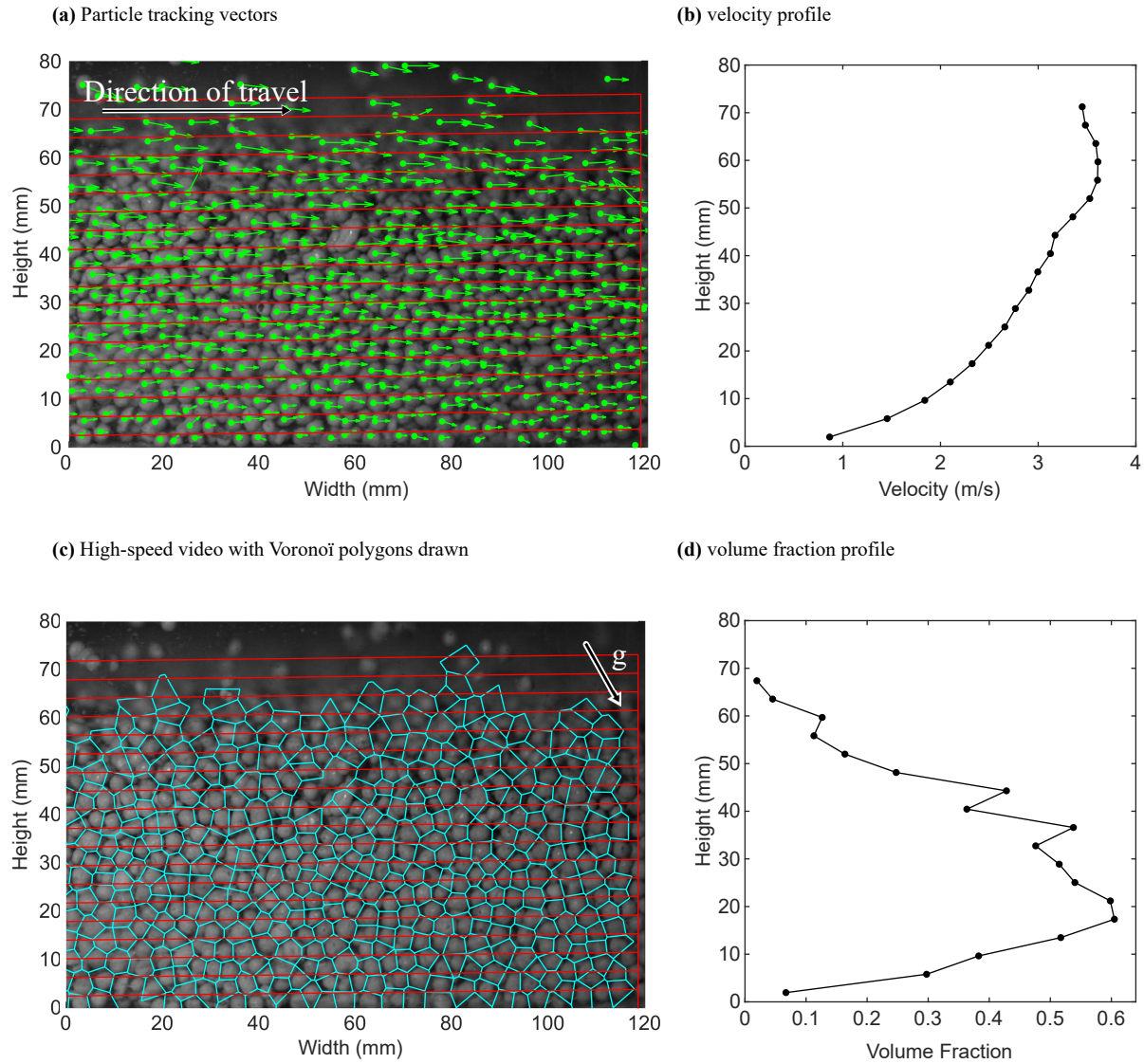


Figure 3. Representative video analysis and calculated profiles using PTV for 0.8 m^3 dry flow at peak flow height, illustrating (a) displacement vectors (green arrows) identified by PTV within bins drawn parallel to flume base (in red), (b) velocity profile calculated from displacement vectors within each bin, (c) Voronoi polygons drawn around particle locations for use in volume fraction estimation method, and (d) estimated volume fraction profile.

281 polygons which share an edge with the analysis area of interest were disregarded, as the
 282 shape of these polygons may have been ‘clipped’ by the analysis area of interest. Before
 283 inclusion into the average, each Voronoï polygon was assessed for size and shape; Voronoï
 284 polygons with areas exceeding 2.5 times the area of an average particle or with a round-
 285 ness parameter ξ below 0.70 were then discarded. Any polygon bordering a polygon which
 286 was discarded due to size or shape was not included in the average.

287 The volume fraction profile (Figure 3d) is estimated by:

$$\frac{\nu}{\nu_{rcp}} = \left(\frac{\xi - \xi_0}{\xi_{rcp} - \xi_0} \right)^\beta$$

288 where indices “rcp” and “0” designate the state of random close packing and the dilute
 289 state, respectively. For random close packing of spheres, $\nu_{rcp} \approx 0.64$ (Allen & Thomas,
 290 1999). Capart et al. (2002) performed a calibration study for volume fractions in the range
 291 $0.20 \leq \nu \leq 0.55$ and found calibration constants $\xi_{rcp} = 0.84$, $\xi_0 = 0.72$, and $\beta = 3.5$.
 292 Volume fractions $\nu \leq 0.20$ are approximated by the point density method, also by Ca-
 293 part et al. This method was developed for the case where particles are observed against
 294 a rigid transparent wall, but calibrated with the average volume fraction in the cell. Thus,
 295 the method is expected to estimate the volume fraction away from the influence of the
 296 rigid wall.

297 As the flow inevitably contained some saltating particles above the flow, a threshold is
 298 required to define what is considered to be the body of the flow. For the purposes of fur-
 299 ther analysis and discussion in this paper, the flow height of the trials was set by the thresh-
 300 old $\nu = 0.20$ over height and time (Figure 4). Some manual adjustments were made
 301 to exclude particles which were not immediately beside the sidewall glass. This was judged
 302 by the shallow depth of field of the camera lens and the incident light. The top of fluid
 303 was manually marked on images at 0.05 second intervals for the wet flows.

304 4 Flow characteristics

305 We begin the comparison of dry and saturated flows through visual observations of flow
 306 structure, velocity, volume fraction, and pore pressure measured at the observation point
 307 near the end of the inclined section of the flume (the ‘CAM1’ location). The times ex-
 308 amined are shown on Figure 4. The 0.8 m³ volume is chosen for this comparison of typ-
 309 ical anatomy of the flows as this source volume exhibits the system of flow regimes dis-
 310 cussed throughout this paper but is not at the extreme of source volumes tested. Later
 311 sections of the manuscript explore the variability observed in larger and smaller volumes
 312 and full analysis of the resulting deposit morphology.

313 4.1 Dry flow

314 The flow regimes within a 0.8 m³ dry flow are revealed by the velocity and volume frac-
 315 tion profiles as it passes the ‘CAM1’ location (Figure 5) at selected times t since door
 316 opening. The initial front of the debris flow is heralded by saltating particles (Figure 5a)
 317 with $\nu \approx 0.2$ and (basal) slip velocity in excess of 2.5 ms⁻¹. A high level of collisional
 318 activity is seen when reviewing the video. As the core approaches (Figure 5b), the vol-
 319 ume fraction increases to approximately $\nu = 0.32$. The bottom of the flow slows and
 320 $\dot{\gamma}$ quickly increases. The slip velocity at $t = 1.74$ s is 1.8 ms⁻¹, while the surface ve-
 321 locity is 4.0 ms⁻¹ with a flow height of 36 mm.

322 The peak flow height comprises a dense ($\nu > 0.49$) core above a collisional base with
 323 a higher magnitude of $\dot{\gamma}$. The peak flow height of approximately 52 mm is visible at $t =$
 324 2.59 s (Figure 5c). The surface velocity is approximately 3.4 ms⁻¹, slower than at $t =$
 325 1.74 s even though the flow height is higher. The slip velocity has reduced further to ap-
 326 proximately 0.9 m s⁻¹.

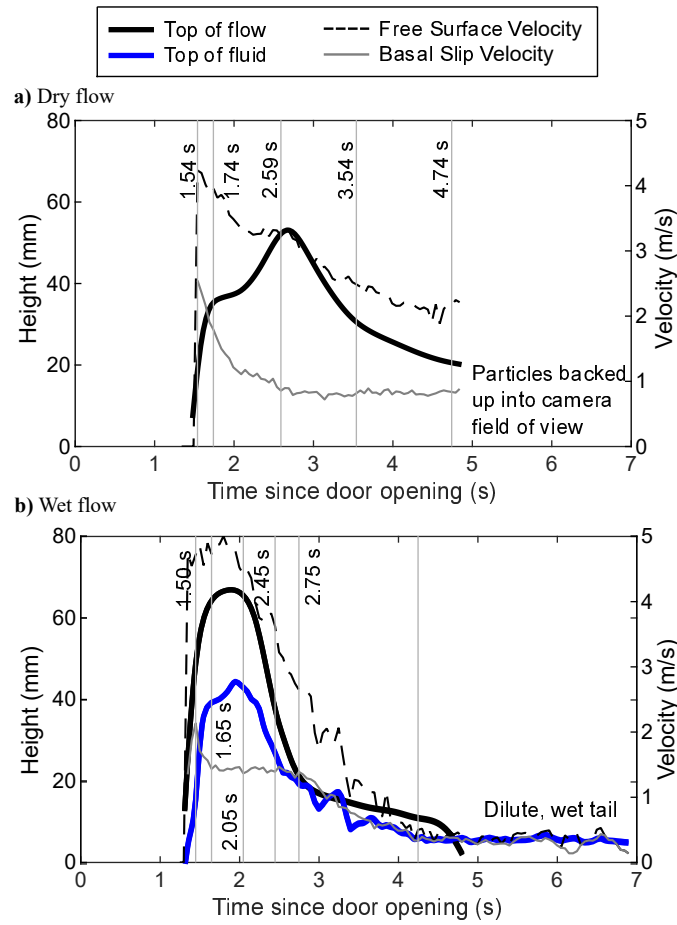


Figure 4. Flow heights (from side view camera) vs time, at ‘CAM1’ location near the end of the inclined section of flume, for representative 0.8 m^3 (a) dry and (b) wet flows. The initially saturated flow is taller, has the majority of the mass biased towards the front of the flow, and has a long thin tail portion. The top of fluid is below the top of flow at the time of peak flow height. The free surface and basal slip velocities are also shown.

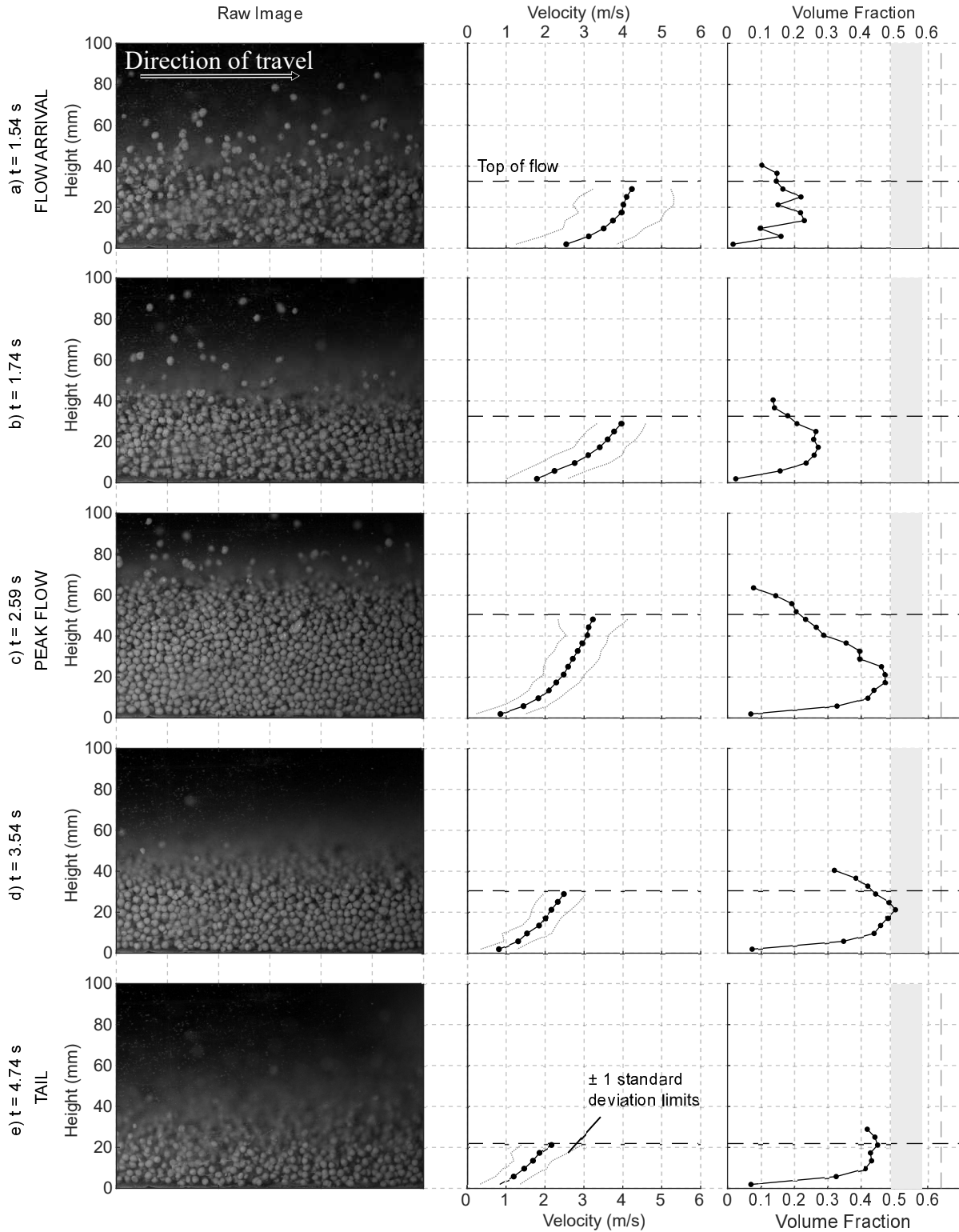


Figure 5. Anatomy of 0.8 m^3 dry flow at end of inclined section of flume ('CAM1'), showing a frame of video, the velocity profile with ± 1 standard deviation limits (in the 0.02 s observation time window), and the volume fraction ν at times (a) $t = 1.54 \text{ s}$, (b) $t = 1.74 \text{ s}$, (c) $t = 2.59 \text{ s}$, (d) $t = 3.54 \text{ s}$, (e) $t = 4.74 \text{ s}$ since door opening.

327 The volume fraction reduces gradually and the pressure at the base reduces after the body
 328 of the flow passes (Figure 5d). At $t = 3.54$ s, ν ranges up to a maximum of 0.51. At
 329 $t = 4.74$ s (Figure 5e), the flow height has reduced to approximately 21 mm and ν has
 330 reduced to approximately 0.28. The slip velocity remains at 0.8 ms^{-1} and the surface
 331 velocity has reduced to 2.2 ms^{-1} . At $t = 4.85$ s, the determination of the velocity for
 332 the 0.8 m^3 flow is not possible as particles at rest begin to back up into the camera's field
 333 of view. The runout morphology for this experiment is discussed in Section 6.

334 4.2 Saturated flow

335 The typical behaviour of a fluid saturated flow is presented in Figure 6 for the 0.8 m^3
 336 volume. The front of the flow arrives before the fluid, similar to the unsaturated gran-
 337 ular front observed in laboratory experiments by Leonardi et al. (2015) and Turnbull et
 338 al. (2015). In the early arrival stages of the core of the flow (Figure 6a), the top of fluid
 339 is seen at an approximate height of 30 mm while the flow height is approximately 43 mm.
 340 The free surface velocity exceeds 4.8 ms^{-1} , faster than the dry flow. The velocity pro-
 341 file shows a very high $\dot{\gamma} \approx 200 \text{ s}^{-1}$ near the flume base and minimal $\dot{\gamma}$ above the top
 342 of fluid. In rigid bed experiments, Armanini et al. (2005) also measured the highest $\dot{\gamma}$
 343 near the base. Here, the flow is dilute, with identified volume fractions typically rang-
 344 ing between 0.3 and 0.4.

345 By $t = 2.05$ s, the flow height and the top of fluid are at their peak (Figure 6c), while
 346 the surface velocity has decreased to 4.5 ms^{-1} . The concentration of shear near the base
 347 of the flow continues. The density is less than the dry flow and is further reduced near
 348 the top of flow. Below the top of fluid, the maximum volume fraction, $\nu = 0.52$. In the
 349 portion of the flow above this, $\nu = 0.21$.

350 The top of fluid is coincident with the surface at $t = 2.75$ s (Figure 6e) as the tail of
 351 the flow passes 'CAM1'. The flow is relatively dilute with $\nu = 0.32$. The slip velocity
 352 reduces from 1.6 ms^{-1} at $t = 2.75$ s to 0.4 ms^{-1} at $t = 4.00$ s, at which time the flow
 353 is only two particles high. This is in stark contrast to the tail end of the dry flows, where
 354 the slip velocity is seen to be relatively constant (Figure 4).

355 Overall, the partitioning into a head section, frictional core, collisional base, and tail sec-
 356 tion is more pronounced for a wet flow than dry flow of the same volume.

357 A similar, repeat, test was carried out for the 0.8 m^3 initially saturated flow, with the
 358 high-speed video camera set at the 'CAM2' location (Figure 2) on the horizontal runout
 359 portion of the flume. The results show that the flow arrives in a dense ($\nu > 0.49$) state
 360 at the residual water content with a free surface speed of approximately 2.6 ms^{-1} (Fig-
 361 ure 7a), which is approximately half that at the time of peak flow at the upstream 'CAM1'
 362 position. The peak flow height is over 100 mm, approximately two-thirds greater than
 363 at 'CAM1'. This shows that the material has laterally compressed following the change
 364 in slope. $\dot{\gamma}$ is highest near the base.

365 The top of fluid rises quickly to 102 mm above the flume base at $t = 2.40$ s (Figure 7b).
 366 A reduction in the volume fraction occurs simultaneously, especially near the top of the
 367 flow. As the core passes and the tail comes into view at $t = 3.00$ s (Figure 7c), the ve-
 368 locity decreases throughout the depth profile. The density increases in the lower portion
 369 of the flow. Later, the flow arrests completely while the tail is in the view of the cam-
 370 era.

371 4.3 Basal fluid pressures

372 During the initially saturated 0.8 m^3 flow, the centreline and side basal fluid pressure
 373 sensors at $x = -0.50$ m show similar peak pressure measurements. This leads to the
 374 conclusion that the flow is sufficiently mature at 'CAM1' to have recovered from the ini-
 375 tial impulse of the granular collapse from the source box. Further down the flume at $x =$
 376 $+1.42$ m, the pressure traces are also generally similar from the centreline location to
 377 the side location.

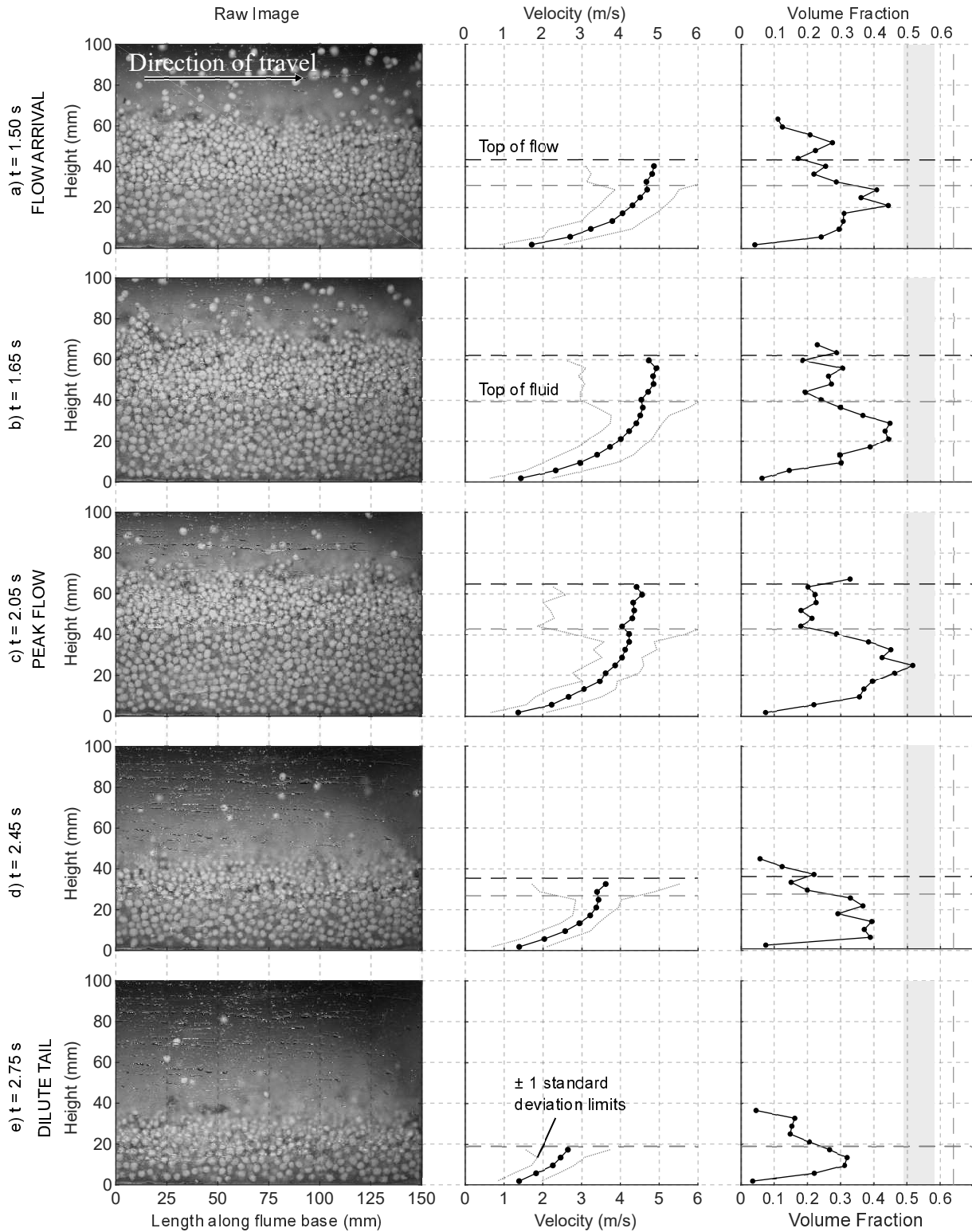


Figure 6. Anatomy of 0.8 m^3 initially saturated flow at end of inclined section of flume ('CAM1') showing a frame of video, the velocity profile with ± 1 standard deviation limits (in the 0.02 s observation time window), and the volume fraction ν at times (a) $t = 1.50 \text{ s}$, (b) $t = 1.65 \text{ s}$, (c) $t = 2.05 \text{ s}$, (d) $t = 2.45 \text{ s}$, (e) $t = 2.75 \text{ s}$ since door opening.

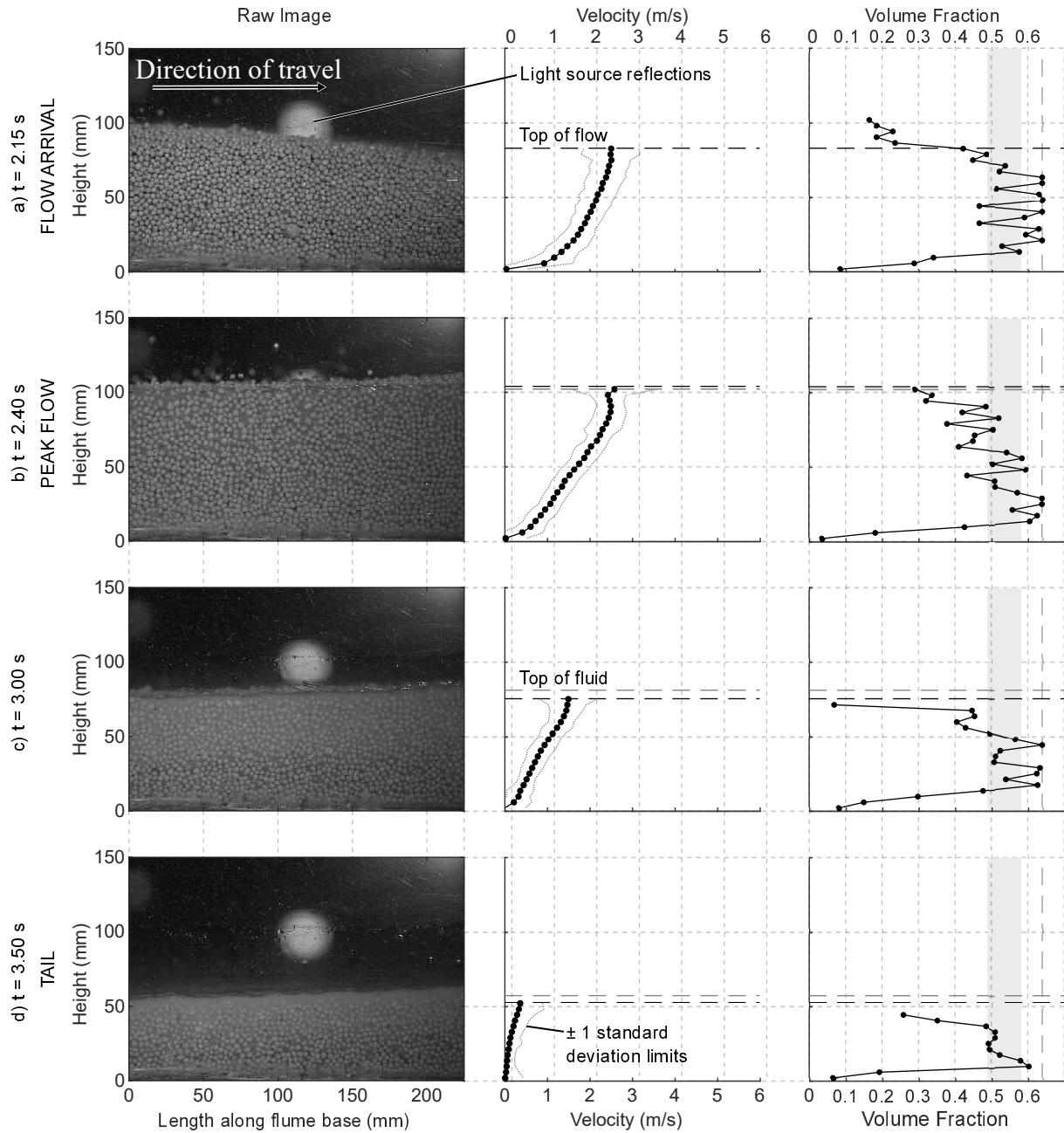


Figure 7. Anatomy of 0.8 m^3 wet flow in horizontal runout section of flume (‘CAM2’) showing a frame of video, the velocity profile with ± 1 standard deviation limits (in the 0.02 s observation time window), and the volume fraction ν at times (a) $t = 2.15 \text{ s}$, (b) $t = 2.40 \text{ s}$, (c) $t = 3.00 \text{ s}$, (d) $t = 3.50 \text{ s}$ since door opening.

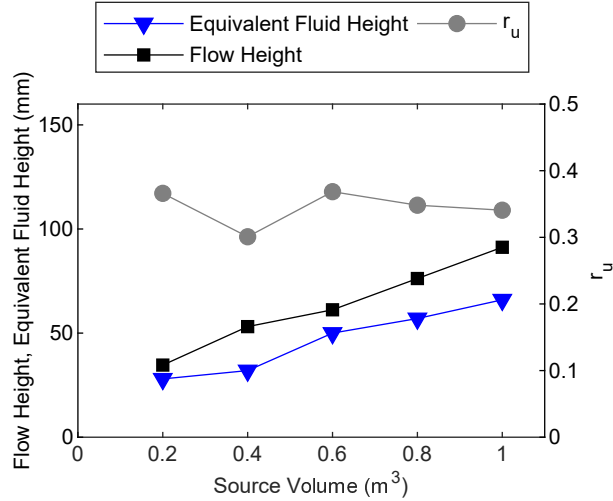


Figure 8. Peak flow heights and fluid pressures observed at $x = -0.50$ m along centreline for initially saturated trials, with equivalent fluid height remaining below flow height over range of source volumes tested. The pore pressure ratio r_u is defined here as the ratio of fluid pressure to the total vertical pressure.

378 The visually-identified top of fluid at the side of the flow can be compared to the mea-
 379 sured basal fluid pressure P at the centre of the flow, expressed as an equivalent bed-
 380 normal fluid height $H = P/\rho_w g \cos \theta$, where the density of water $\rho_w = 1000 \text{ kg} \cdot \text{m}^3$,
 381 the slope angle $\theta = 30^\circ$ and $g = 9.81 \text{ m} \cdot \text{s}^{-2}$. Here, the height H is similar between
 382 the visually-identified flow height (at the side wall) to the ultrasonic flow height sensor
 383 (at the centreline). The equivalent height of the basal fluid pressure is equal to the the
 384 height of the fluid, indicating that the matrix fluid pressures did not exceed the equiv-
 385 alent hydrostatic regime.

386 The basal fluid pressures consistently increase across the four sensors installed on the
 387 horizontal runout portion. The highest pressures observed are at the furthest distance
 388 from the release box. This is attributed to the increasing flow height as the front of the
 389 flow slows and the rear of the flow cascades over. Good agreement is seen between the
 390 equivalent fluid height from the sensor at $x = +2.68$ m and the top of fluid. The wet
 391 flow is subject to contraction during the arrest phase but the basal fluid pressures do not
 392 increase above hydrostatic.

393 5 Effect of varying source volume

394 In this section, we expand on the comparison of dry and initially saturated flows using
 395 observations of flow thickness, velocity, volume fraction, and pore pressure measured at
 396 the observation point near the end of the inclined section of the flume (the ‘CAM1’ lo-
 397 cation) for source volumes ranging between 0.2 to 1.0 m³. This comparison is conducted
 398 to look at grain-scale mechanisms controlling the flow structure that may give rise to scale
 399 effects with flow volume.

400 5.1 Flow thicknesses and fluid pressures

401 As source volume increased through the tested range of 0.2 to 1.0 m³, the observed max-
 402 imum flow thickness at $x = -0.50$ m (‘CAM1’) increased from 38 to 51 mm for the dry
 403 flows and from 30 to 79 mm for the initially saturated flows.

As shown in Figure 8 at $x = -0.50$ m, the maximum equivalent bed-normal fluid height (as calculated in Section 4.3) is equal to the peak flow height for the range of initially saturated source volumes tested. This suggests the matrix fluid pressures did not exceed the equivalent hydrostatic regime. The pore pressure ratio r_u , defined here as the ratio of fluid pressure to the total vertical pressure, ranges between [0.36 : 0.44].

5.2 Behaviour at peak flow height

In Figure 9, the time of peak flow height passing ‘CAM1’ is selected as a basis for comparison between the flows. This is the time when the flow is at its thickest and most dense state, and therefore the transport rate of mass is highest. A review of the profiles, discussed in detail below, provides information on the state of flow at the end of the incline as well as the partitioning of particles between highly shearing, lightly shearing, and collisional regimes.

At the time of peak flow height passing ‘CAM1’, the velocity profile of each of the initially saturated flows (“wet”) is faster than that of the dry flows. The overall velocity of the wet flows increases as source volume increases, with the top of the core of the 1.0 m^3 flow attaining a speed exceeding 5.0 ms^{-1} . Wet flows of all volumes are each seen to have a very high $\dot{\gamma}$ near the base of the flow. The opposite is noted for the dry flows, which are seen to be slower for each height in the flow as source volume increases.

Two forms of velocity profile were fit to each flow as best possible. Firstly, in the form of Bagnold (1954):

$$u(y) = a \left[h^{3/2} - (h - y)^{3/2} \right] + b$$

where h is the flow height and a , b are best-fit constants. Secondly, a logarithmic velocity profile $u(y) = c \ln y + d$, where c , d are best-fit constants, representing a fully turbulent hydraulic flow. The velocity profiles of the dry flows are well represented by the Bagnold profiles, as expected for dense granular flows following the $\mu(I)$ rheology (Forterre & Pouliquen, 2008). For the wet flows, the fit quality of the Bagnold profile decreases as flow volume increases. The logarithmic profile has a higher quality of fit than the Bagnold profile above 0.4 m^3 , and matches well through 0.4 to 0.8 m^3 range. The fit quality decreases for the 1.0 m^3 wet flow, suggesting a variation of flow regime with depth. The shape of the velocity profiles, with nonzero basal slip velocity and a decreasing $\dot{\gamma}$ with increasing height above the base, is similar to the solid bed flows of Armanini et al. (2005) (Figure S1, supporting information). Velocity profiles of natural debris flows on a non-erodible bed measured by Nagl et al. (2020) indicate a nonzero basal slip velocity and a mostly concave-up velocity profile during a flow event, with complex deposition and re-mobilization of material during a sequence of surges.

At ‘CAM2’ after the change in slope, the 0.8 m^3 wet flow maintains this highly shearing flow which transports material (at residual water content) to the front of the flow. By comparison, the 0.4 m^3 wet flow displays minimal shearing at the same location.

Across the range of source volumes, the volume fraction profiles at the time of peak height passing ‘CAM1’ (Figure 9) for the dry flows display a similar shape as the 0.8 m^3 flow discussed above. The maximum volume fraction of the core increases with source volume. Each volume of wet flows displays a similar shape as the 0.8 m^3 flow, with a reduction in volume fraction above the top of fluid. The 0.2 through 0.6 m^3 dry flows each are entirely in a collisional regime when assessed by volume fraction. The 0.8 and 1.0 m^3 dry flows each have portions exceeding $\nu = 0.583$, indicating a frictional regime. While the maximum volume fractions of the wet flows increase slightly with source volume, the wet flows each have a lower maximum volume fraction than the dry flows of the same source volume and all remain in a collisional regime. For the dry flows, the volume fraction near the base is relatively consistent over the range of 0.2 to 0.8 m^3 . For the 1.0 m^3

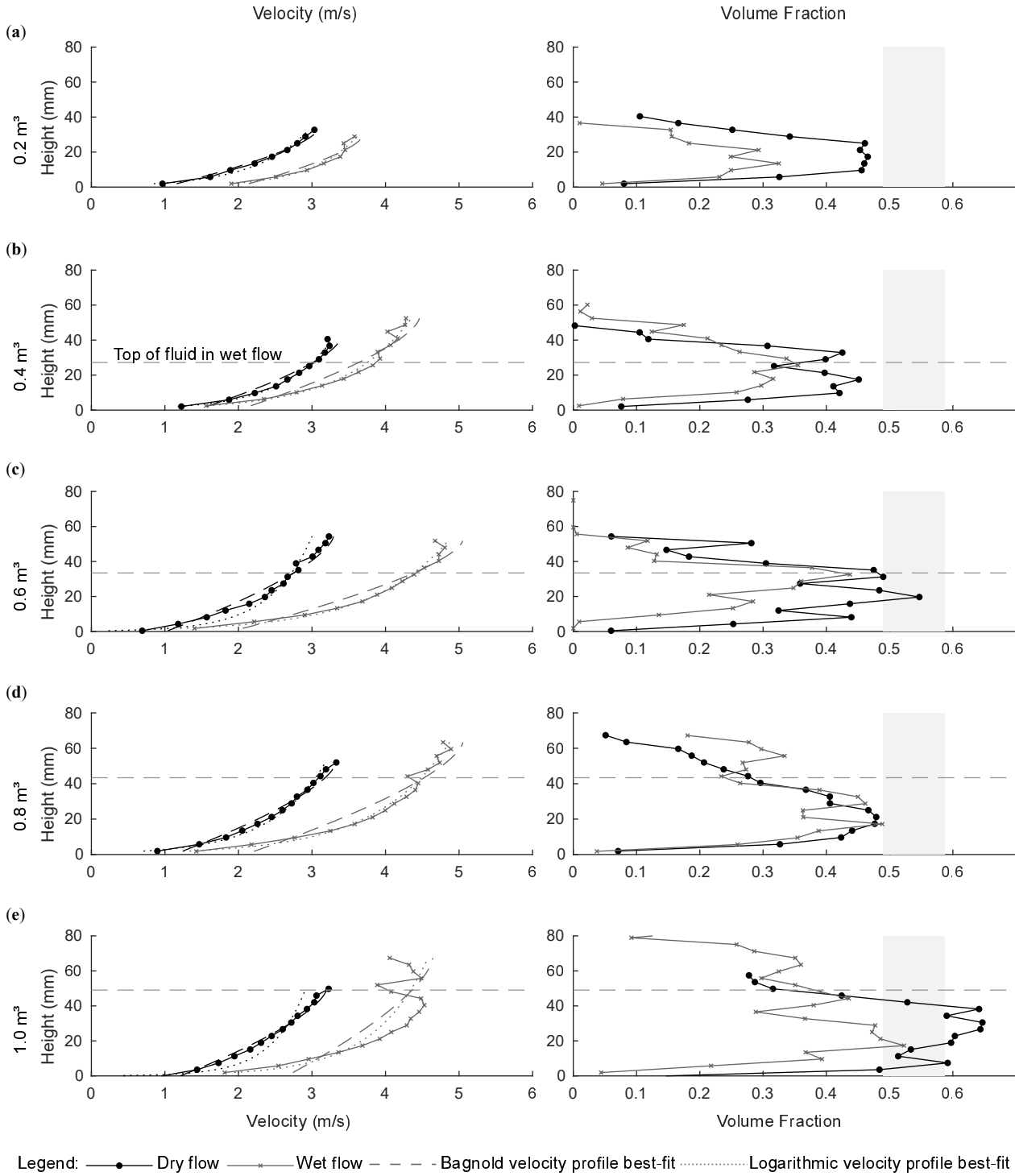


Figure 9. Comparison of depth profiles of streamwise velocity and volume fraction at the time of maximum flow height for (a) 0.2 m^3 to (e) 1.0 m^3 flows in 0.2 m^3 increments. Best-fits of Bagnoldian and logarithmic velocity profiles are shown in dashed and dotted lines, respectively. The shading in the volume fraction plot represents the dense collisional regime ($0.49 \leq \nu \leq 0.583$).

452 flow, the dense region is seen to extend down to near the flume base, suggesting that the
 453 increased confining pressure of the thicker frictional core has suppressed the collisional
 454 base. The wet flows displayed a reduction in volume fraction near the base over the range
 455 of source volumes, coincident with a high $\dot{\gamma}$.

456 The basal and free surface velocities and depth-averaged volume fractions are detailed
 457 for each trial in Table S1, in the supporting information. Using these parameters, all flows
 458 were classified as collisional flows by the Inertial Number I (e.g. Turnbull et al., 2015;
 459 Forterre & Pouliquen, 2008). The strong variation of $\dot{\gamma}$ with depth seen in the wet flows
 460 suggests that the Inertial Number varies with depth in the flows, and classification from
 461 a depth-averaged Inertial Number does not reliably describe the grain-scale behaviour
 462 seen in the wet flows.

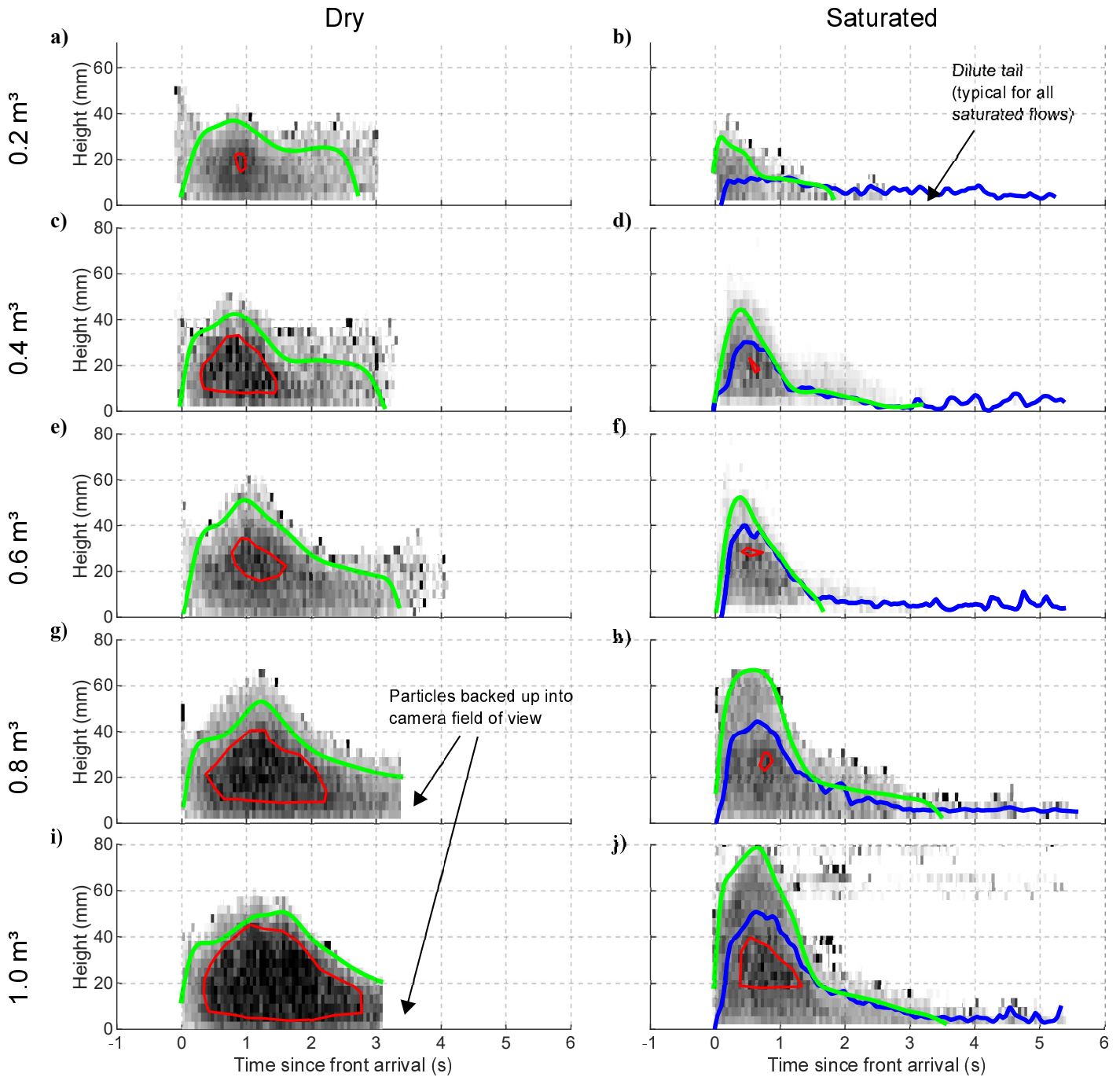
463 5.3 Longitudinal distribution of regimes

464 We note that the core region of the initially saturated flows appears to enter an efficient
 465 mode of transport that increases in velocity with flow thickness, to a greater extent than
 466 would be expected according to Bagnoldian theory. Hence, the size of this core region
 467 relative to the total flow size is examined here. The partitioning into regimes along the
 468 length of the flow from head to tail can be assessed through plots of the measured quan-
 469 tities for each analysis interval and depth bin. Figure 10 shows the volume fraction re-
 470 sults and Figure 11 shows the velocity results in a contour plot format where the con-
 471 tour lines represent isovelocity lines. $\dot{\gamma}$ can be inferred from the vertical distance between
 472 the isovelocity contour lines: isovelocity lines closer together represent a higher shear rate.
 473 Where the lines are parallel to the x-axis, that portion of the velocity profile is constant
 474 with time.

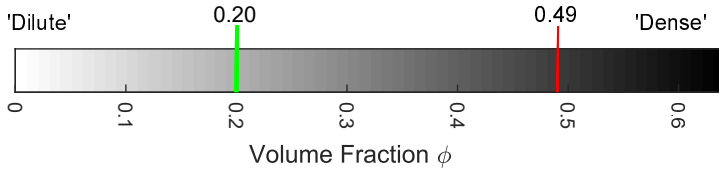
475 The volume fraction of the dry flows (Figure 10) shows partitioning of the flow into a
 476 dilute, saltating head preceding the front, a dense core where volume fraction increases
 477 with source volume, and a gradual reduction of volume fraction towards the tail. Dur-
 478 ing this transition period, the velocity results show only gradual changes with time (Fig-
 479 ure 11). Geometric similarity of the flow height over time is evident across the range of
 480 source volumes and the change in flow height between core and tail is gradual. In con-
 481 trast, for the wet flows the regime of the tail is distinct from the core for both volume
 482 fraction and velocity (Figure 10 and Figure 11, respectively).

483 The initially saturated flows each display a period with near-constant velocity in the base
 484 of the flow (Figure 11), with the duration of this increasing with source volume. Only
 485 a short period of near-constant velocity in the base is observed within the 0.2 m³ flow,
 486 increasing to 0.9 s for the 1.0 m³ flow. The maximum $\dot{\gamma}$ near the base does not vary sig-
 487 nificantly with source volume, suggesting that the wet flows find a preferred, efficient state
 488 of flow. The velocity profiles remain near-constant as the flow height reduces until seem-
 489 ingly falling below a critical threshold where the velocity abruptly reduces and the tail
 490 begins. This phenomenon is also visible on a plot of the slip velocity over time from the
 491 flow front (Figure 12) as a distinct plateau for the wet flows but not for the dry flows.

492 The decrease in velocity from core to tail was greater for the wet flows than the dry flows.
 493 An effect for the deceleration of the wet flows is thought to be due to surface tension be-
 494 tween the liquid phase with the flume base and sidewalls. At this stage, the tail portions
 495 of the initially saturated flows are slow moving and of low volume fraction and minimal
 496 thickness. Some ceramic beads remained on the flume surface at the end of the exper-
 497 iments until the remnant water evaporated. The material partitioned to this slow-moving
 498 tail would reduce the volume available to be transported at high speed in the core sec-
 499 tion of the flow. This is in accordance with the description of ‘starving’ avalanches by
 500 Bartelt et al. (2007).



Colourmap scale represents Volume Fraction as determined by Voronoi-based method



Legend

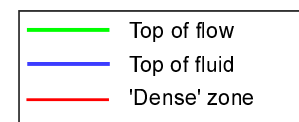
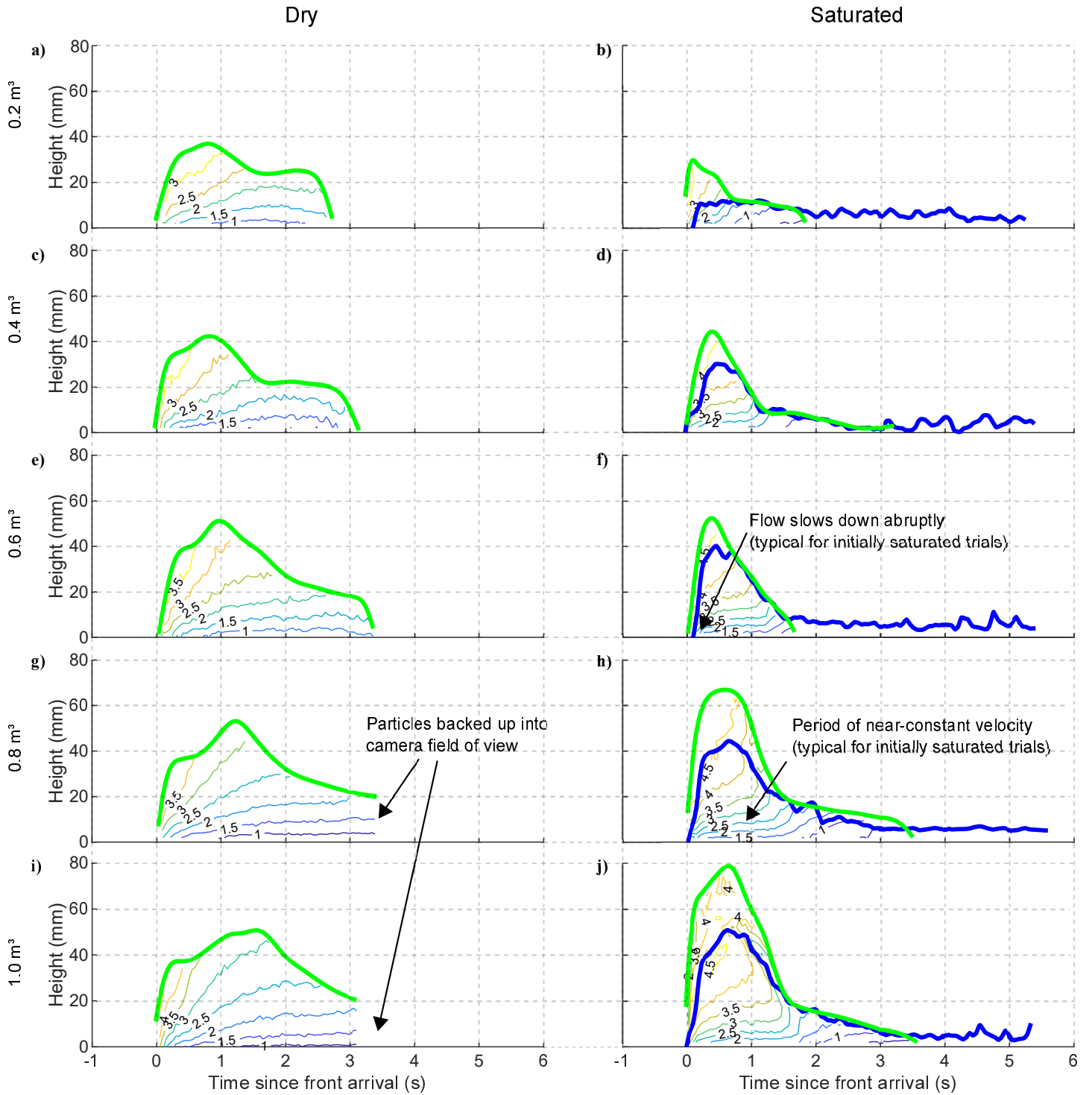


Figure 10. Height (y)-Time (x)-Volume Fraction (color scale) plots for dry and saturated trials over the range of source volumes, illustrating the formation of a dense granular core for dry flows and a comparatively dilute core for wet flows. Both flows exhibit a reduction in volume fraction near the rigid flume base.



Contour lines represent streamwise flow velocity as determined by PTV method

Legend

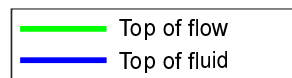


Figure 11. Height (y)-Time (x)-Velocity (color scale) plots for dry and initially saturated trials over the range of source volumes, illustrating a period of near-constant velocity near the base of the flume for the initially saturated state, suggesting that the flows find a preferred, efficient state of flow for translation and until the core height reduces below a critical threshold.

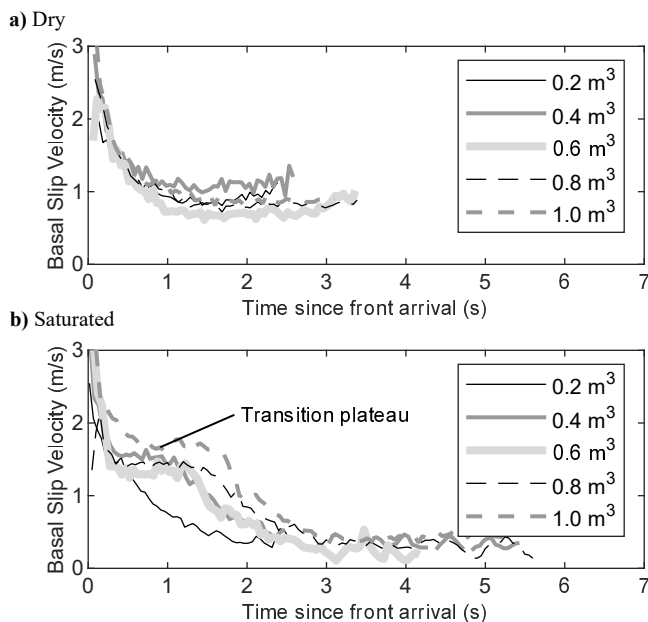


Figure 12. Comparison of basal slip velocities at end of incline for (a) dry trials illustrating the gradual decline in basal slip velocity and (b) initially saturated trials, illustrating a ‘step’ phenomenon where the velocity remains constant while the core passes, then quickly reduces to a slow speed ($<0.5\text{ ms}^{-1}$) for the tail.

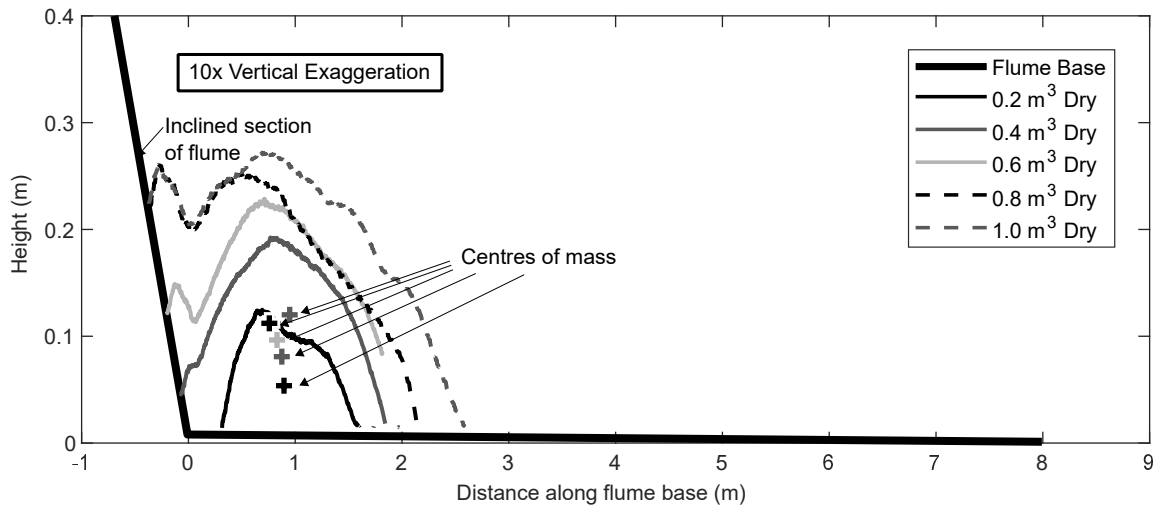
501 6 Variation of morphology of resultant deposit with source volume

502 In the previous section, observations at the grain-scale revealed localized shearing at the
 503 base and evolution of volume fraction zones with flow height. In this section, we explore
 504 the changes in bulk behaviour, as reflected in the deposit morphology, for the varied source
 505 volumes.

506 The deposit morphology for each of the five dry and five saturated flow volumes, cap-
 507 tured using LIDAR scanning, is presented in Figure 13. The profile of deposit morphol-
 508 ogy illustrates geometrical similarity (centre-of-mass travel distance, shape and slope an-
 509 gles of the deposit) over the range of source volumes for dry flows. In contrast, the ini-
 510 tially saturated flows display markedly increased runout distances as source volume in-
 511 creases. Runout statistics, illustrated schematically in Figure 1a, can be used to sum-
 512 marize the resultant deposit morphologies (Figure 14). The frontal extents of the flow
 513 are considered in Heim’s Ratio H/L (Figure 14a). Heim’s Ratio remains relatively con-
 514 stant for dry flows but decreases significantly for initially saturated flows, indicating in-
 515 creased mobility with volume. Parez & Aharonov (2015) decompose the runout into trans-
 516 lation of the centre-of-mass, related to an apparent friction coefficient, and forward spread
 517 S_f ahead of the centre-of-mass (Figure 14b). A slight increase in the forward spreading
 518 distance is seen for dry flows, commensurate with geometric similitude. For the initially
 519 saturated flows, a much larger increase of the forward spreading distance with volume
 520 occurs, the majority of which is from translation of the centre-of-mass.

521 The travel angle statistics summarize the translation of the centre-of-mass (Figure 14c),
 522 with a lower travel angle indicating a general increase in mobility. For the dry tests, a
 523 relatively consistent travel angle of 27.1° to 28.1° was calculated over the range of source
 524 volumes tested. For the wet tests, the travel angle reduced significantly from 25.7° for
 525 a source volume of 0.2 m^3 to 20.1° for a source volume of 1.0 m^3 . This marked decrease

(a) Dry trials



(b) Initially saturated trials

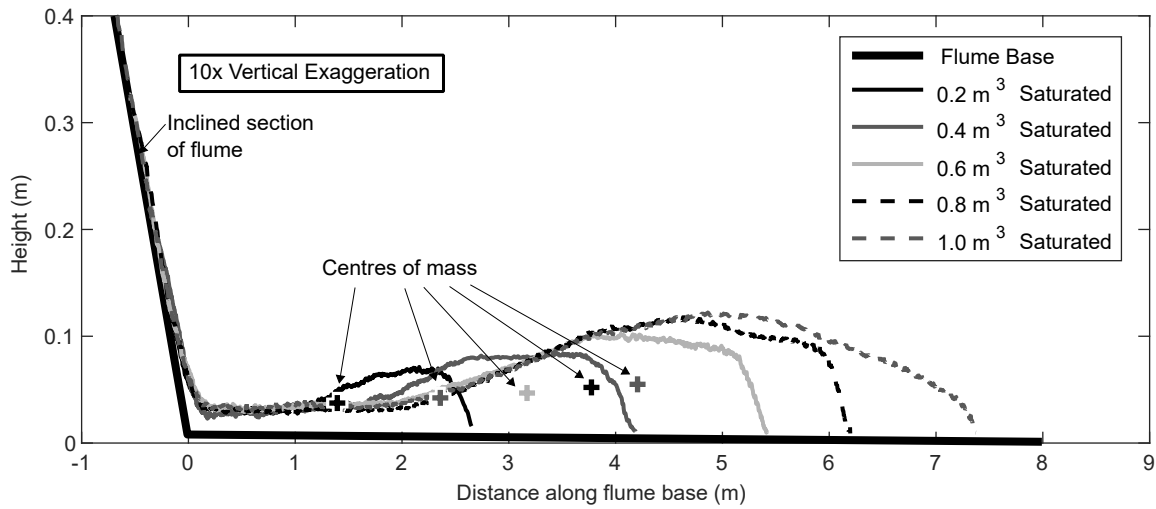


Figure 13. Comparison of resultant deposit morphology profiles for (a) dry and (b) initially saturated trials, with calculated centres of mass indicated.

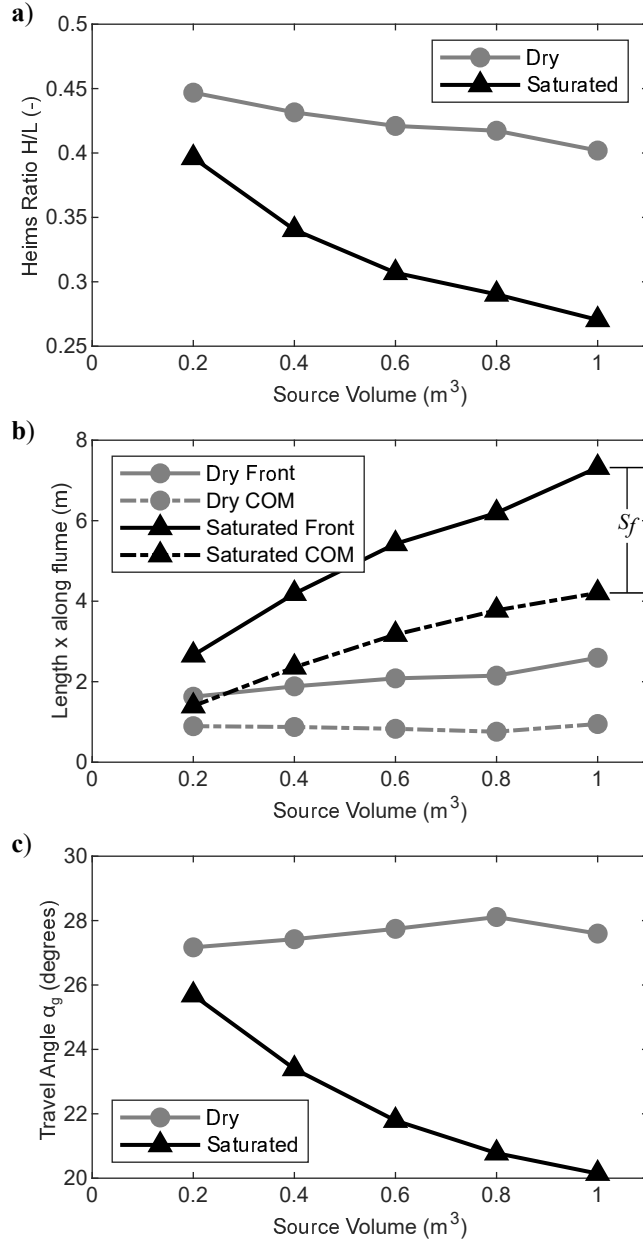


Figure 14. Comparison of summary statistics of mobility, showing (a) Heim's ratio from top of source volume to distal reach of deposit, (b) position of front extent of deposit and centre-of-mass of deposit, illustrating the relative contributions of each to total runout, and (c) travel angle between centres of mass.

526 indicates that one or more physical processes within the rheology of the wet flows are
527 affected by experiment size.

528 7 Conclusions

529 A series of monodisperse granular flows was released within a large laboratory flume to
530 define the effect of landslide volume on the runout distance and the relative contribu-
531 tions of translation and spreading in the end member case of high permeability debris.
532 Both dry and initially saturated states were tested and the source volume was system-
533 atically varied from 0.2 to 1.0 m³ in 0.2 m³ increments. The use of high permeability
534 debris retained the possible influences of particle buoyancy and fluid drag but was con-
535 firmed to not result in basal fluid pressures that exceed hydrostatic conditions. The tests
536 exhibited marked differences in runout distance and flow regimes as observed by high-
537 speed video between dry and initially water saturated conditions. The initially saturated
538 flows displayed an increase in flow velocity and runout distance as flow source volume
539 increased. This increase in total mobility was seen to come more from translation of the
540 centre-of-mass than spreading at the front.

541 For particles considered as a frictional continuum, the effect of interstitial fluid is through
542 reduction in the contact stresses between particles. In this case where the interstitial fluid
543 pressures did not exceed hydrostatic conditions, the effect would be limited to particle
544 buoyancy and not subject to scaling with flow thickness. Fluid drag can also occur if the
545 interstitial fluid is travelling at a different speed than the particles.

546 The results show that the lower portions of the wet flows have decreased in volume frac-
547 tion significantly and have entered a collisional regime. $\dot{\gamma}$ is highest in the collisional zone
548 near the base. The variation in flow speed and translation distance may be caused by
549 partitioning of the source volume into generally 1) a highly shearing base, 2) a core sec-
550 tion above and 3) a slow tail section. Energy is only expended by the flow when $\dot{\gamma}$ is nonzero.
551 Energy expenditure is concentrated in the base of the flow and the tail section starves
552 the flow of fluid and particles as the flume surface is wet and the particles remain by cap-
553 illary forces. The remainder of the source volume is transported in the core very quickly
554 with little energy expenditure, and is the prime contributor to the long runout distances
555 observed. This system of flow regimes is considered to be a preferred, efficient state of
556 flow.

557 The scaling effects are postulated to arise when varying source volumes are not split into
558 these regimes proportionally. The experiments showed the highly shearing base to be of
559 similar height across the series of wet flows and the tail sections appeared similar as well.

560 The data show that the flow resistance of fluid-saturated flows may be defined by par-
561 ticle collisions and interactions with interstitial fluid on a local scale and preclude depth-
562 averaged or continuum approaches. Physical experiments linking particulate behaviour
563 to bulk response are required to fully validate and calibrate conceptual and numerical
564 models of collisional and multiphase behaviour.

565 The results suggest some potential applications to granular mass flows in the field, e.g.
566 debris flows. The shape of the velocity profiles (Figure 9) for the identical sediment mix-
567 ture are useful to constrain an appropriate rheology to describe several aspects of the
568 flow behavior of both dry and wet granular flows. The shape of the velocity profile is es-
569 pecially useful for choosing an appropriate rheology (or friction relation) used in depth-
570 averaged runout models of debris flows. Such models (e.g. Barnhart et al. 2021) are used
571 for hazard mapping, interpretation of recent events and also for impact calculations for
572 designing mitigation measures. The shape of the velocity profile is necessary to increase
573 the accuracy of the depth-averaged momentum predicted by such models. Experiments
574 to evaluate the influence of basal roughness on the velocity profile, which is beyond the
575 scope of this study, would provide an additional data set to better understand the role
576 of basal friction and basal slip on the shape of the velocity profiles. The observation that

577 the velocity profile changes with water content is also of interest for accurately deter-
 578 mining the volume of a debris flow from depth recordings in cases where independent
 579 observations of the volume are unavailable. Solutions to this problem are rare, and un-
 580 til now the rheology (or more simply the friction relation) of a debris flow is assumed
 581 to be constant over the duration of an event (e.g. Schlunegger et al. 2009), or the vari-
 582 ation of velocity with depth and time within a flow is not considered, resulting in sys-
 583 tematic errors in estimating the instantaneous discharge and volume of a debris flow.

584 Flume experiments will remain useful for debris flow research for the foreseeable future.
 585 This data provides additional support to the conclusion that flow thickness matters, par-
 586 ticularly for fluid saturated flows. This study begins to address the paucity of such ex-
 587 periments through the publication of a unique dataset that combines the detailed grain-
 588 scale visual observations of flow structure, velocity, and volume fraction, with the ob-
 589 served consequences in terms of effective friction and debris spreading. This unique dataset
 590 is publicly available on the Scholarsportal Dataverse repository to serve as a well-defined
 591 test scenario to assess the role of interstitial fluid in numerical runout models of debris
 592 flows.

593 Open Research

594 The data used in this research are archived in the Queen’s University Dataverse (<https://doi.org/10.5683/SP3/1ZCU>)

595 Acknowledgments

596 This project is the result of a Leverhulme Trust International Network Grant (#IN-2016-
 597 041) “The Rosetta Stone Network: Physical testing towards a common understanding
 598 of debris flows”. Funding for the first author provided by a NSERC Discovery Grant to
 599 the last author. The first author would like to thank Natalie Arpin, Branna MacDougall,
 600 Erica Treflik-Body, Megan McKellar, Andrea Walsh, Artur Sass Braga, Joshua Cogh-
 601 lan, Graeme Boyd, Hal Stephens and Richard Foley for their ideas and assistance in the
 602 laboratory.

603 References

- 604 Allen, S. M., & Thomas, E. L. (1999). *The structure of materials* (Vol. 44). Wiley
 605 New York.
- 606 Alonso, E. E., Zervos, A., & Pinyol, N. M. (2016). Thermo-poro-mechanical anal-
 607 ysis of landslides: from creeping behaviour to catastrophic failure. *Géotechnique*,
 608 *66*(3), 202–219. doi: 10.1680/jgeot.15.lm.006
- 609 Ancy, C. (2007). Plasticity and geophysical flows: A review. *Journal of Non-*
 610 *Newtonian Fluid Mechanics*, *142*(1-3), 4–35. doi: 10.1016/j.jnnfm.2006.05.005
- 611 Ancy, C., & Evesque, P. (2000). Frictional-collisional regime for granular suspen-
 612 sion flows down an inclined channel. *Physical Review E*, *62*(6), 8349–8360. doi: 10
 613 .1103/physreve.62.8349
- 614 Armanini, A. (2013). Granular flows driven by gravity. *Journal of Hydraulic Re-*
 615 *search*, *51*(2), 111–120. doi: 10.1080/00221686.2013.788080
- 616 Armanini, A., Capart, H., Fraccarollo, L., & Larcher, M. (2005). Rheological strat-
 617 ification in experimental free-surface flows of granular–liquid mixtures. *Journal of*
 618 *Fluid Mechanics*, *532*, 269–319. doi: 10.1017/s0022112005004283
- 619 Bagnold, R. (1954). Experiments on a gravity-free dispersion of large solid spheres
 620 in a newtonian fluid under shear. *Proceedings of the Royal Society of London. Ser-*
 621 *ies A. Mathematical and Physical Sciences*, *225*(1160), 49–63. doi: 10.1098/rspa
 622 .1954.0186
- 623 Barnhart, K. R., Jones, R. P., George, D. L., McArdell, B. W., Rengers, F. K., Sta-
 624 ley, D. M., & Kean, J. W. (2021). Multi-model comparison of computed debris
 625 flow runout for the 9 january 2018 montecito, california post-wildfire event. *Jour-*
 626 *nal of Geophysical Research: Earth Surface*, *126*(12). doi: 10.1029/2021jf006245

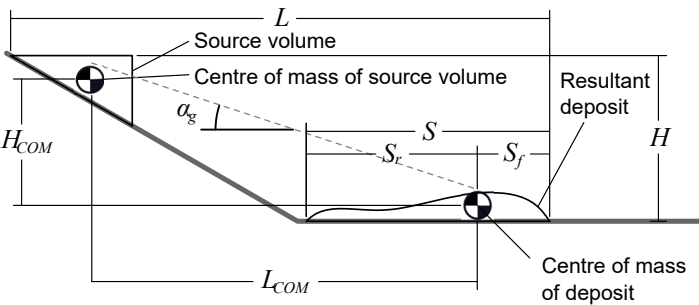
- 627 Bartelt, P., Buser, O., & Platzler, K. (2007). Starving avalanches: Frictional mech-
 628 anisms at the tails of finite-sized mass movements. *Geophysical Research Letters*,
 629 *34*(20). doi: 10.1029/2007gl031352
- 630 Bowman, E., Take, W., Rait, K., & Hann, C. (2012). Physical models of rock
 631 avalanche spreading behaviour with dynamic fragmentation. *Canadian Geotechni-
 632 cal Journal*, *49*(4), 460–476. doi: 10.1139/t2012-007
- 633 Brevis, W., Niño, Y., & Jirka, G. H. (2010). Integrating cross-correlation and relax-
 634 ation algorithms for particle tracking velocimetry. *Experiments in Fluids*, *50*(1),
 635 135–147. doi: 10.1007/s00348-010-0907-z
- 636 Bryant, S. K., Take, W. A., & Bowman, E. T. (2015). Observations of grain-scale
 637 interactions and simulation of dry granular flows in a large-scale flume. *Canadian
 638 Geotechnical Journal*, *52*(5), 638–655. doi: 10.1139/cgj-2013-0425
- 639 Caballero, L., Sarocchi, D., Soto, E., & Borselli, L. (2014). Rheological changes
 640 induced by clast fragmentation in debris flows. *Journal of Geophysical Research:
 641 Earth Surface*, *119*(9), 1800–1817. doi: 10.1002/2013jf002942
- 642 Capart, H., Young, D. L., & Zech, Y. (2002). Voronoï imaging methods for the mea-
 643 surement of granular flows. *Experiments in Fluids*, *32*(1), 121–135. doi: 10.1007/
 644 s003480200013
- 645 Chialvo, S., Sun, J., & Sundaresan, S. (2012). Bridging the rheology of granu-
 646 lar flows in three regimes. *Physical Review E*, *85*(2). doi: 10.1103/physreve.85
 647 .021305
- 648 Coombs, S. (2018). *A physical investigation of the flow structure and mobility be-
 649 haviour of collisional granular landslides* (mathesis). Queen’s University.
- 650 Coombs, S., Apostolov, A., Take, W. A., & Benoit, J. (2019). Mobility of dry granu-
 651 lar flows of varying collisional activity quantified by smart rock sensors. *Canadian
 652 Geotechnical Journal*. doi: 10.1139/cgj-2018-0278
- 653 Corominas, J. (1996). The angle of reach as a mobility index for small and large
 654 landslides. *Canadian Geotechnical Journal*, *33*(2), 260–271. doi: 10.1139/t96-005
- 655 Dade, W. B., & Huppert, H. E. (1998). Long-runout rockfalls. *Geology*, *26*(9), 803.
 656 doi: 10.1130/0091-7613(1998)026<0803:lrr>2.3.co;2
- 657 de Haas, T., Braat, L., Leuven, J. R. F. W., Lokhorst, I. R., & Kleinhans, M. G.
 658 (2015). Effects of debris flow composition on runout, depositional mechanisms,
 659 and deposit morphology in laboratory experiments. *Journal of Geophysical Re-
 660 search: Earth Surface*, *120*(9), 1949–1972. doi: 10.1002/2015jf003525
- 661 Fischer, J.-T., Kaitna, R., Heil, K., & Reiweger, I. (2018). The heat of the flow:
 662 Thermal equilibrium in gravitational mass flows. *Geophysical Research Letters*,
 663 *45*(20). doi: 10.1029/2018gl079585
- 664 Forterre, Y., & Pouliquen, O. (2008). Flows of dense granular media. *Annual Review
 665 of Fluid Mechanics*, *40*(1), 1–24. doi: 10.1146/annurev.fluid.40.111406.102142
- 666 Gollin, D., Brevis, W., Bowman, E. T., & Shepley, P. (2017). Performance of PIV
 667 and PTV for granular flow measurements. *Granular Matter*, *19*(3). doi: 10.1007/
 668 s10035-017-0730-9
- 669 Goren, L., & Aharonov, E. (2007). Long runout landslides: The role of frictional
 670 heating and hydraulic diffusivity. *Geophysical Research Letters*, *34*(7). doi: 10
 671 .1029/2006gl028895
- 672 Hotta, N. (2012). Basal interstitial water pressure in laboratory debris flows over a
 673 rigid bed in an open channel. *Natural Hazards and Earth System Sciences*, *12*(8),
 674 2499–2505. doi: 10.5194/nhess-12-2499-2012
- 675 Hungr, O. (1995). A model for the runout analysis of rapid flow slides, debris flows,
 676 and avalanches. *Canadian Geotechnical Journal*, *32*(4), 610–623. doi: 10.1139/t95
 677 -063
- 678 Hürlimann, M., McArdell, B. W., & Rickli, C. (2015). Field and laboratory analysis
 679 of the runout characteristics of hillslope debris flows in switzerland. *Geomorphol-
 680 ogy*, *232*, 20–32. doi: 10.1016/j.geomorph.2014.11.030

- 681 Iverson, R. M. (1997). The physics of debris flows. *Reviews of Geophysics*, *35*(3),
682 245–296. doi: 10.1029/97rg00426
- 683 Iverson, R. M. (2015). Scaling and design of landslide and debris-flow experiments.
684 *Geomorphology*, *244*, 9–20. doi: 10.1016/j.geomorph.2015.02.033
- 685 Iverson, R. M., Logan, M., LaHusen, R. G., & Berti, M. (2010). The perfect debris
686 flow? aggregated results from 28 large-scale experiments. *Journal of Geophysical*
687 *Research*, *115*(F3). doi: 10.1029/2009jf001514
- 688 Jenkins, J. T. (2007). Dense inclined flows of inelastic spheres. *Granular Matter*,
689 *10*(1), 47–52. doi: 10.1007/s10035-007-0057-z
- 690 Jenkins, J. T., & Savage, S. B. (1983). A theory for the rapid flow of identical,
691 smooth, nearly elastic, spherical particles. *Journal of Fluid Mechanics*, *130*(-1),
692 187. doi: 10.1017/s0022112083001044
- 693 Kaitna, R., Dietrich, W. E., & Hsu, L. (2014). Surface slopes, velocity profiles and
694 fluid pressure in coarse-grained debris flows saturated with water and mud. *Jour-*
695 *nal of Fluid Mechanics*, *741*, 377–403. doi: 10.1017/jfm.2013.675
- 696 Kaitna, R., Palucis, M. C., Yohannes, B., Hill, K. M., & Dietrich, W. E. (2016).
697 Effects of coarse grain size distribution and fine particle content on pore fluid
698 pressure and shear behavior in experimental debris flows. *Journal of Geophysical*
699 *Research: Earth Surface*, *121*(2), 415–441. doi: 10.1002/2015jf003725
- 700 Kessler, M., Heller, V., & Turnbull, B. (2020). Grain Reynolds Number scale effects
701 in dry granular slides. *Journal of Geophysical Research: Earth Surface*, *125*(1).
702 doi: 10.1029/2019jf005347
- 703 Lanzoni, S., Gregoretti, C., & Stancanelli, L. M. (2017). Coarse-grained debris
704 flow dynamics on erodible beds. *Journal of Geophysical Research: Earth Surface*,
705 *122*(3), 592–614. doi: 10.1002/2016jf004046
- 706 Legros, F. (2002). The mobility of long-runout landslides. *Engineering Geology*,
707 *63*(3-4), 301–331. doi: 10.1016/s0013-7952(01)00090-4
- 708 Leonardi, A., Cabrera, M., Wittel, F. K., Kaitna, R., Mendoza, M., Wu, W., & Her-
709 rmann, H. J. (2015). Granular-front formation in free-surface flow of concentrated
710 suspensions. *Physical Review E*, *92*(5). doi: 10.1103/physreve.92.052204
- 711 Lun, C. K. K. (1991). Kinetic theory for granular flow of dense, slightly inelastic,
712 slightly rough spheres. *Journal of Fluid Mechanics*, *233*, 539–559. doi: 10.1017/
713 s0022112091000599
- 714 Lun, C. K. K., & Savage, S. B. (1986). The effects of an impact velocity dependent
715 coefficient of restitution on stresses developed by sheared granular materials. *Acta*
716 *Mechanica*, *63*(1-4), 15–44. doi: 10.1007/bf01182538
- 717 Mangeney, A., Roche, O., Hungr, O., Mangold, N., Faccanoni, G., & Lucas, A.
718 (2010). Erosion and mobility in granular collapse over sloping beds. *Journal of*
719 *Geophysical Research*, *115*(F3). doi: 10.1029/2009jf001462
- 720 McArdell, B. W., Bartelt, P., & Kowalski, J. (2007). Field observations of basal
721 forces and fluid pore pressure in a debris flow. *Geophysical Research Letters*,
722 *34*(7). doi: 10.1029/2006gl029183
- 723 McDougall, S. (2017). 2014 canadian geotechnical colloquium: Landslide runout
724 analysis — current practice and challenges. *Canadian Geotechnical Journal*,
725 *54*(5), 605–620. doi: 10.1139/cgj-2016-0104
- 726 Nagl, G., Hübl, J., & Kaitna, R. (2020). Velocity profiles and basal stresses in nat-
727 ural debris flows. *Earth Surface Processes and Landforms*, *45*(8), 1764–1776. doi:
728 10.1002/esp.4844
- 729 Parez, S., & Aharonov, E. (2015). Long runout landslides: a solution from granular
730 mechanics. *Frontiers in Physics*, *3*. doi: 10.3389/fphy.2015.00080
- 731 Pastor, M., Blanc, T., Haddad, B., Drempevic, V., Morles, M. S., Dutto, P., ...
732 Merodo, J. A. F. (2014). Depth averaged models for fast landslide propagation:
733 Mathematical, rheological and numerical aspects. *Archives of Computational*
734 *Methods in Engineering*, *22*(1), 67–104. doi: 10.1007/s11831-014-9110-3

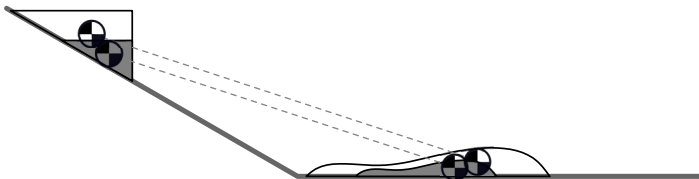
- 735 Pudasaini, S. P., Wang, Y., & Hutter, K. (2005). Modelling debris flows down gen-
 736 eral channels. *Natural Hazards and Earth System Sciences*, *5*(6), 799–819. doi: 10
 737 .5194/nhess-5-799-2005
- 738 Raymond, G. P. (2002). Reinforced ballast behaviour subjected to repeated load.
 739 *Geotextiles and Geomembranes*, *20*(1), 39–61. doi: 10.1016/s0266-1144(01)00024
 740 -3
- 741 Rickenmann, D. (2011). Runout prediction methods. In O. Hungr & M. Jakob
 742 (Eds.), *Debris-flow hazards and related phenomena* (pp. 305–324). Springer Berlin
 743 Heidelberg.
- 744 Schlunegger, F., Badoux, A., McArdell, B. W., Gwerder, C., Schnydrig, D., Rieke-
 745 Zapp, D., & Molnar, P. (2009). Limits of sediment transfer in an alpine debris-
 746 flow catchment, illgraben, switzerland. *Quaternary Science Reviews*, *28*(11-12),
 747 1097–1105. doi: 10.1016/j.quascirev.2008.10.025
- 748 Shugar, D. H., Jacquemart, M., Shean, D., Bhushan, S., Upadhyay, K., Sattar, A.,
 749 ... Westoby, M. J. (2021). A massive rock and ice avalanche caused the 2021
 750 disaster at chamoli, indian himalaya. *Science*, *373*(6552), 300-306. Retrieved
 751 from <https://www.science.org/doi/abs/10.1126/science.abh4455> doi:
 752 10.1126/science.abh4455
- 753 Staron, L., & Lajeunesse, E. (2009). Understanding how volume affects the mo-
 754 bility of dry debris flows. *Geophysical Research Letters*, *36*(12). doi: 10.1029/
 755 2009gl038229
- 756 Taylor-Noonan, A. M., Gollin, D., Bowman, E. T., & Take, W. A. (2021). The influ-
 757 ence of image analysis methodology on the calculation of granular temperature for
 758 granular flows. *Granular Matter*, *23*(4). doi: 10.1007/s10035-021-01153-y
- 759 Tayyebi, S. M., Pastor, M., & Stickle, M. M. (2021). Two-phase SPH numerical
 760 study of pore-water pressure effect on debris flows mobility: Yu Tung debris flow.
 761 *Computers and Geotechnics*, *132*, 103973. doi: 10.1016/j.compgeo.2020.103973
- 762 Tsubaki, T., Hashimoto, H., & Suetsugi, T. (1983). Interparticle stresses and charac-
 763 teristics of debris flow. *Journal of Hydrosience and Hydraulic Engineering*, *1*(2),
 764 67–82.
- 765 Turnbull, B., Bowman, E. T., & McElwaine, J. N. (2015). Debris flows: Experiments
 766 and modelling. *Comptes Rendus Physique*, *16*(1), 86–96. doi: 10.1016/j.crhy.2014
 767 .11.006
- 768 Voight, B., & Faust, C. (1982). Frictional heat and strength loss in some rapid land-
 769 slides. *Géotechnique*, *32*(1), 43–54. doi: 10.1680/geot.1982.32.1.43
- 770 Walter, F., Amann, F., Kos, A., Kenner, R., Phillips, M., de Preux, A., ... Bo-
 771 nanomi, Y. (2020). Direct observations of a three million cubic meter rock-slope
 772 collapse with almost immediate initiation of ensuing debris flows. *Geomorphology*,
 773 *351*, 106933. doi: 10.1016/j.geomorph.2019.106933
- 774 Zhou, G. G. D., Li, S., Song, D., Choi, C. E., & Chen, X. (2018). Depositional
 775 mechanisms and morphology of debris flow: physical modelling. *Landslides*, *16*(2),
 776 315–332. doi: 10.1007/s10346-018-1095-9

Figure 1.

(a) definitions of landslide geometry statistics



(b) travel angle invariant with source volume



(c) travel angle variant with source volume

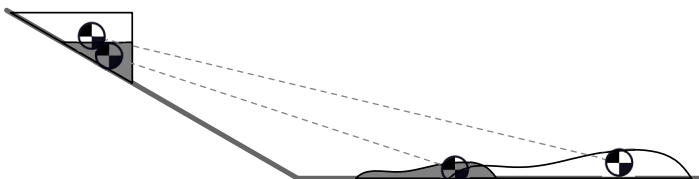


Figure 2.

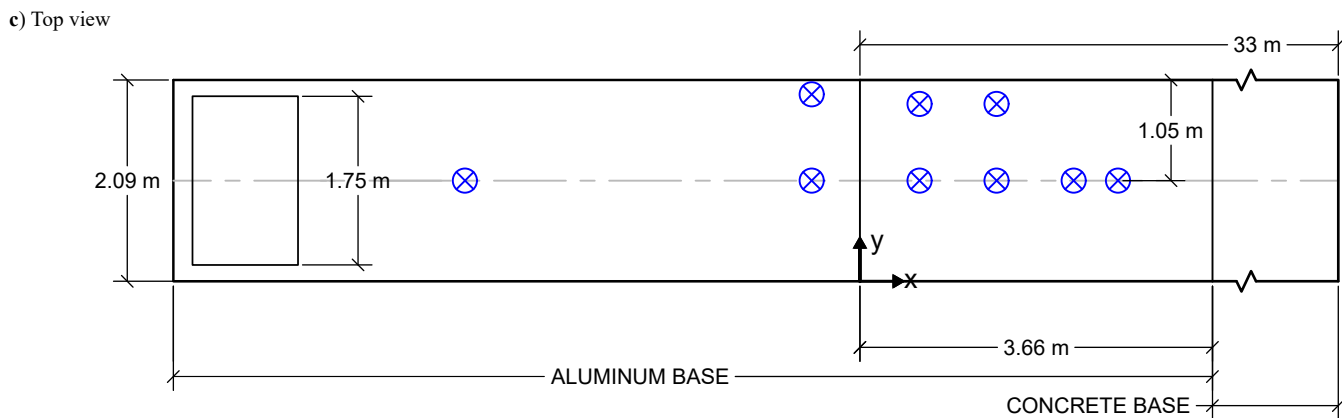
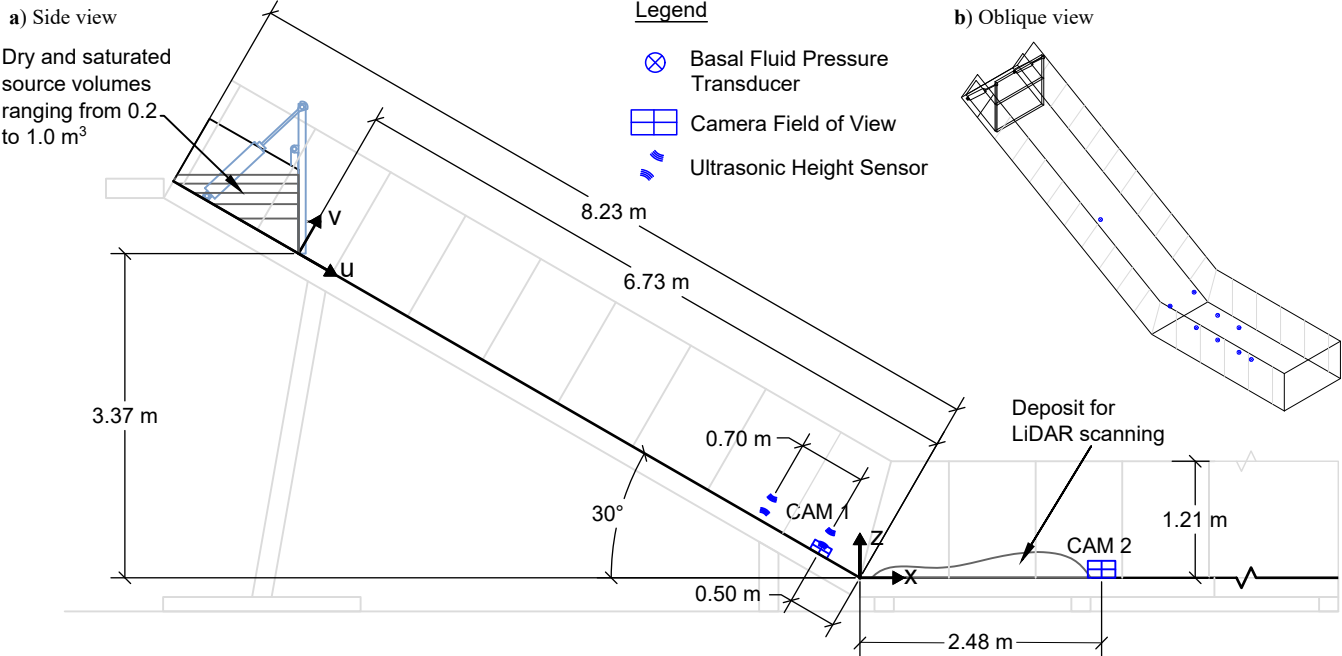


Figure 3.

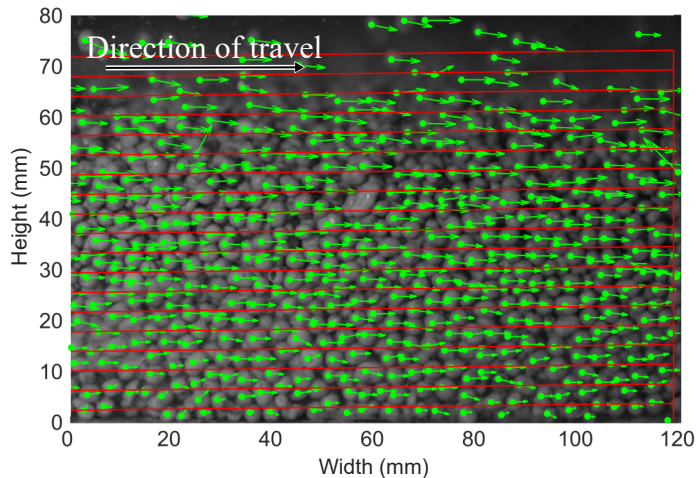
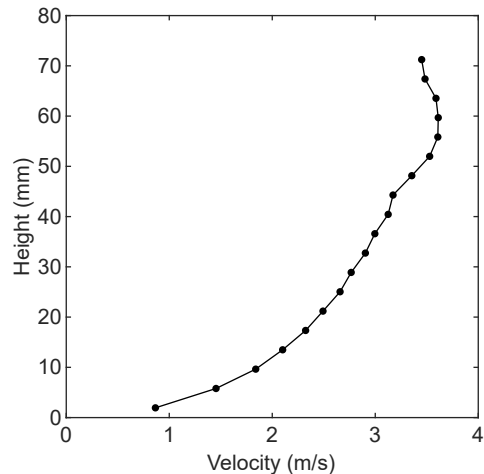
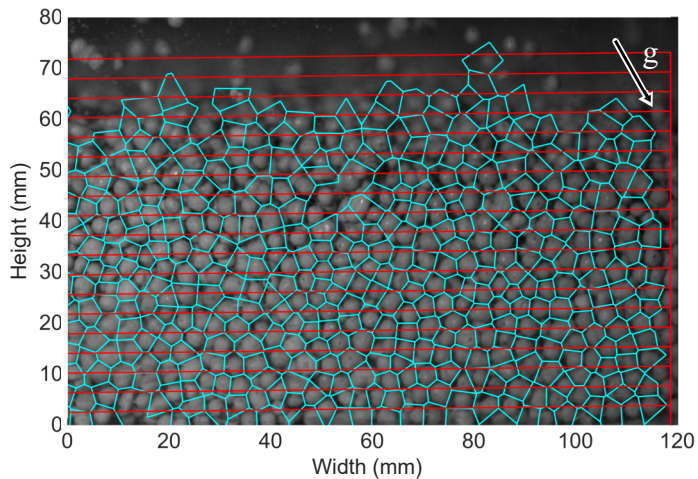
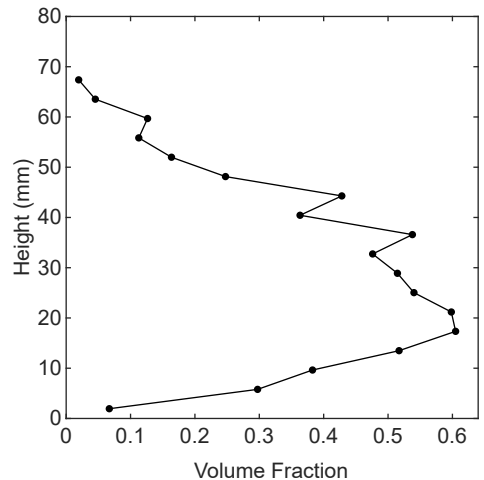
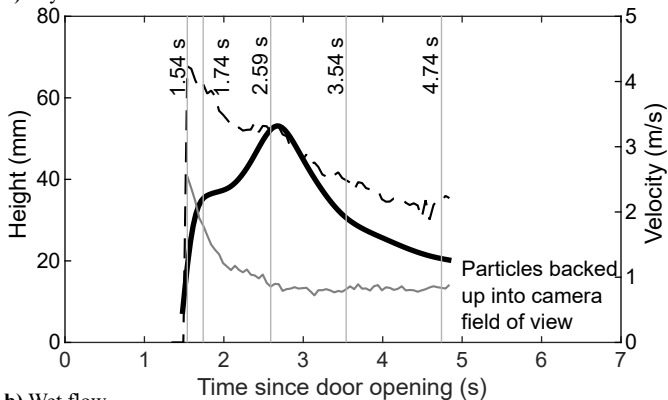
(a) Particle tracking vectors**(b)** velocity profile**(c)** High-speed video with Voronoi polygons drawn**(d)** volume fraction profile

Figure 4.



a) Dry flow



b) Wet flow

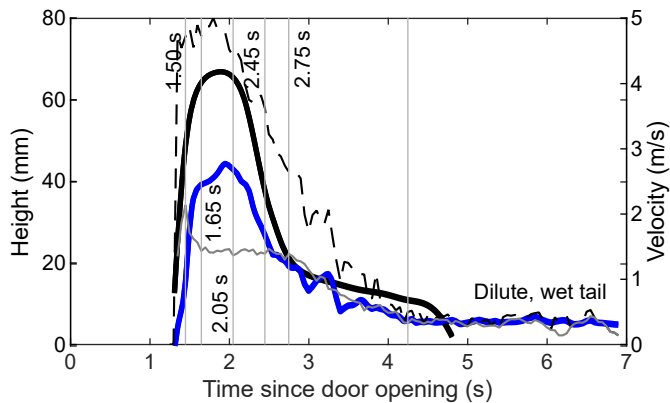


Figure 5.

Figure 6.

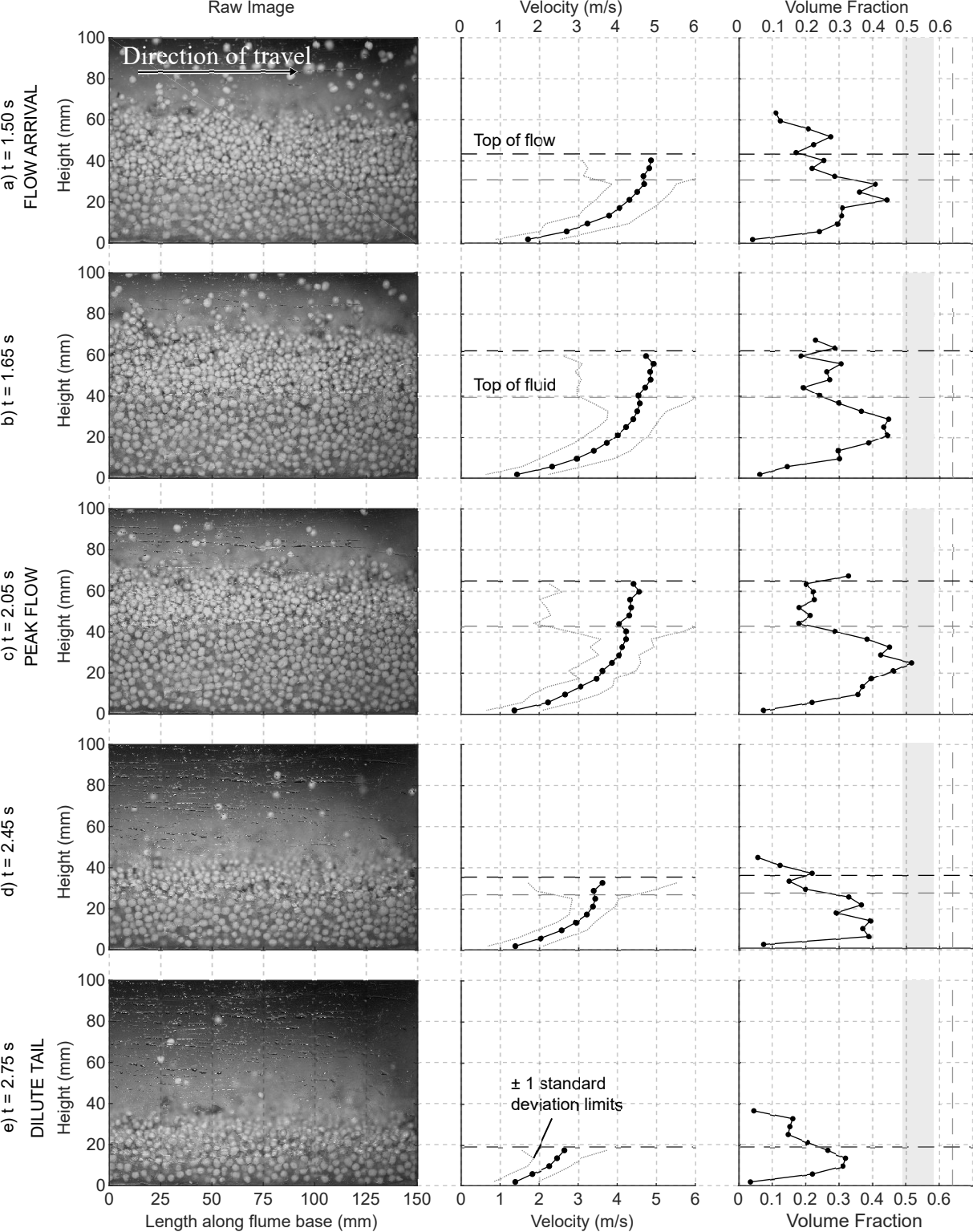


Figure 7.

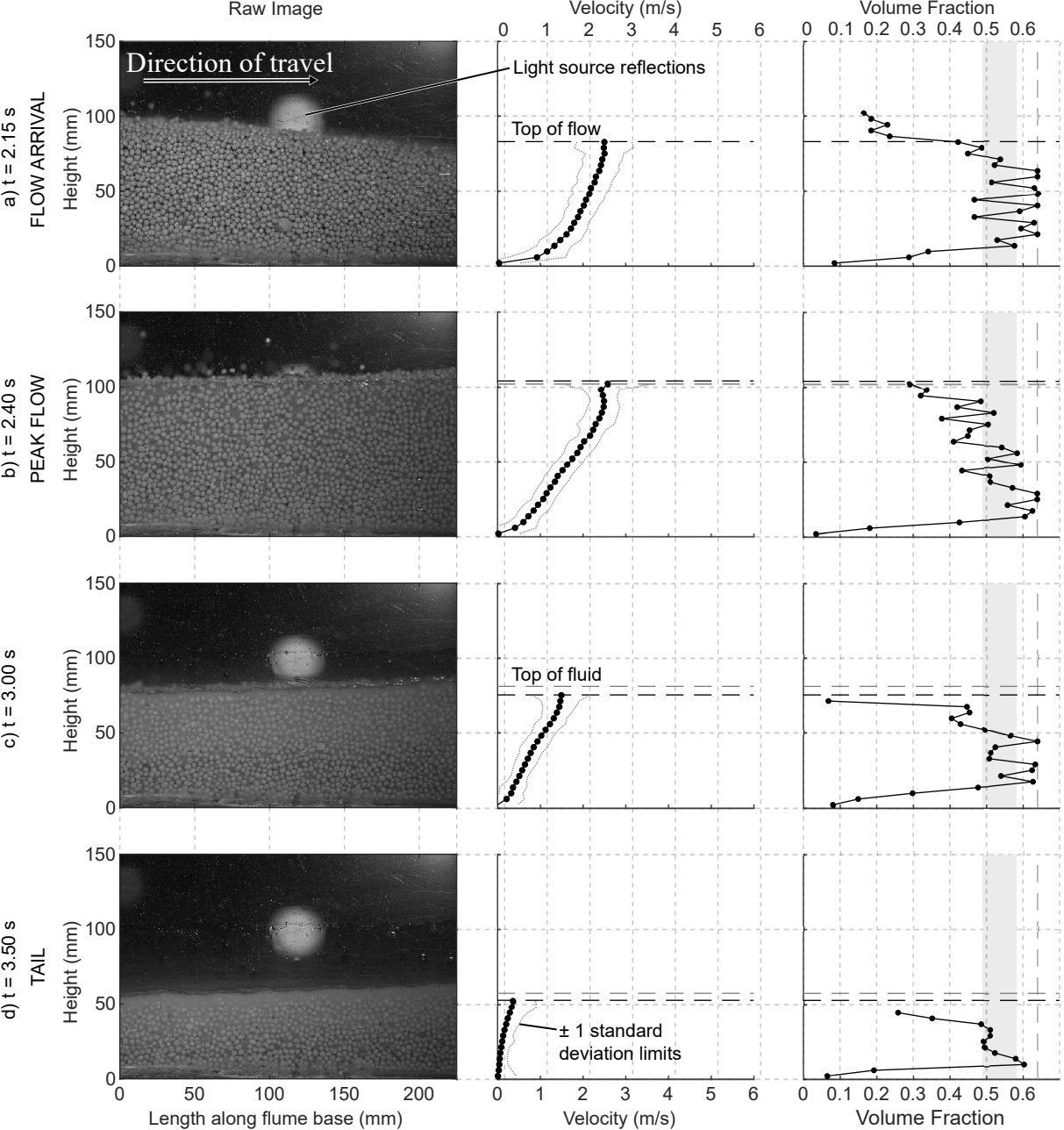


Figure 8.

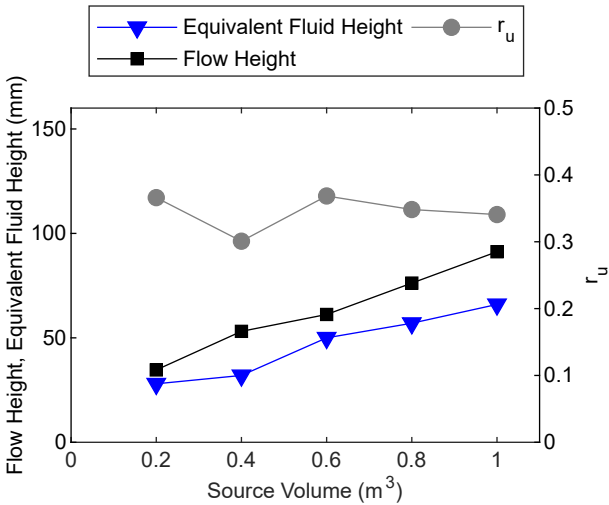
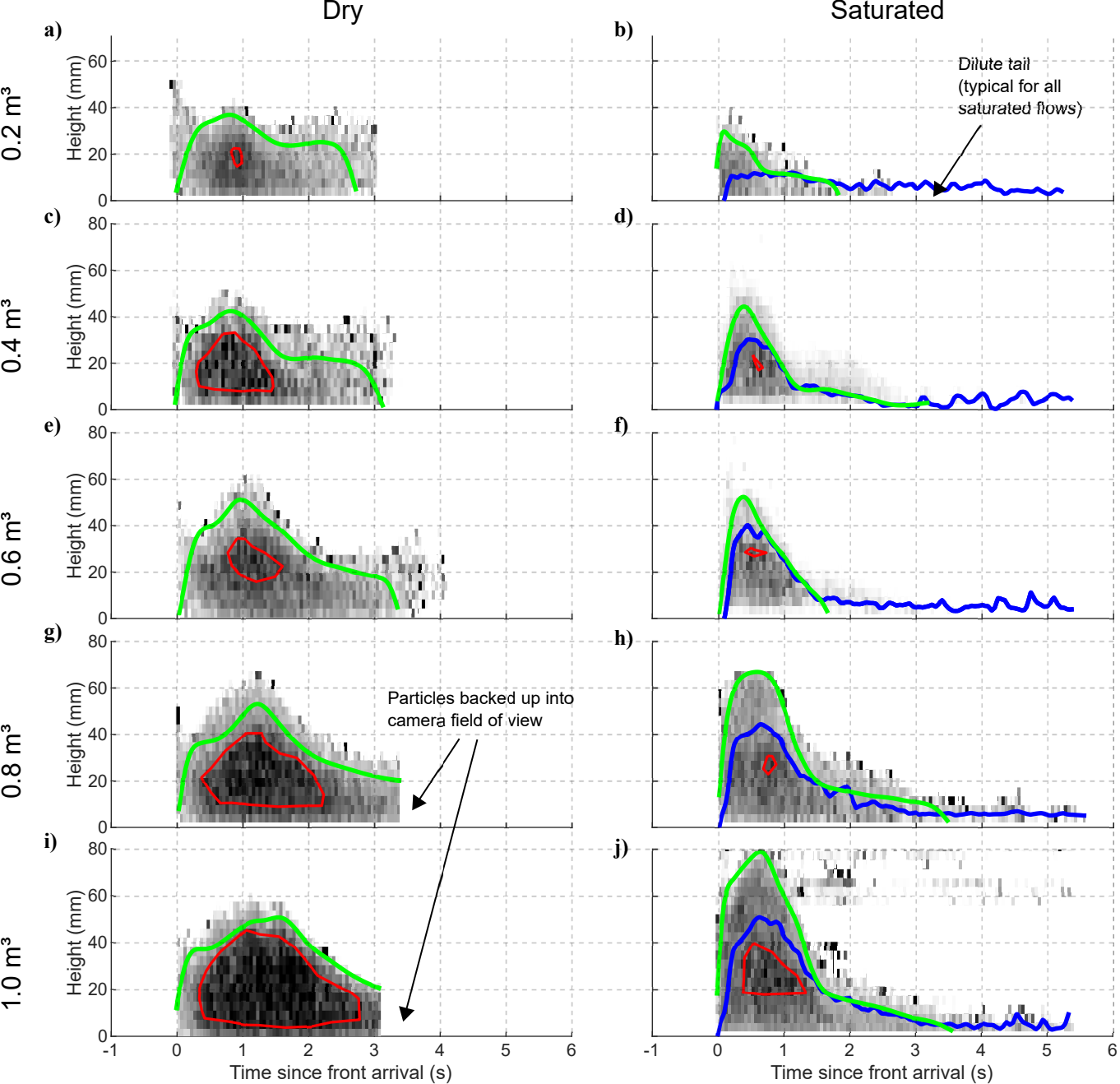
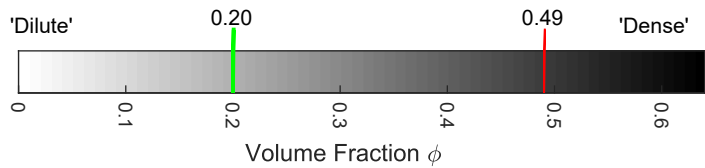


Figure 9.

Figure 10.



Colourmap scale represents Volume Fraction as determined by Voronoi-based method



Legend

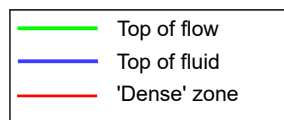
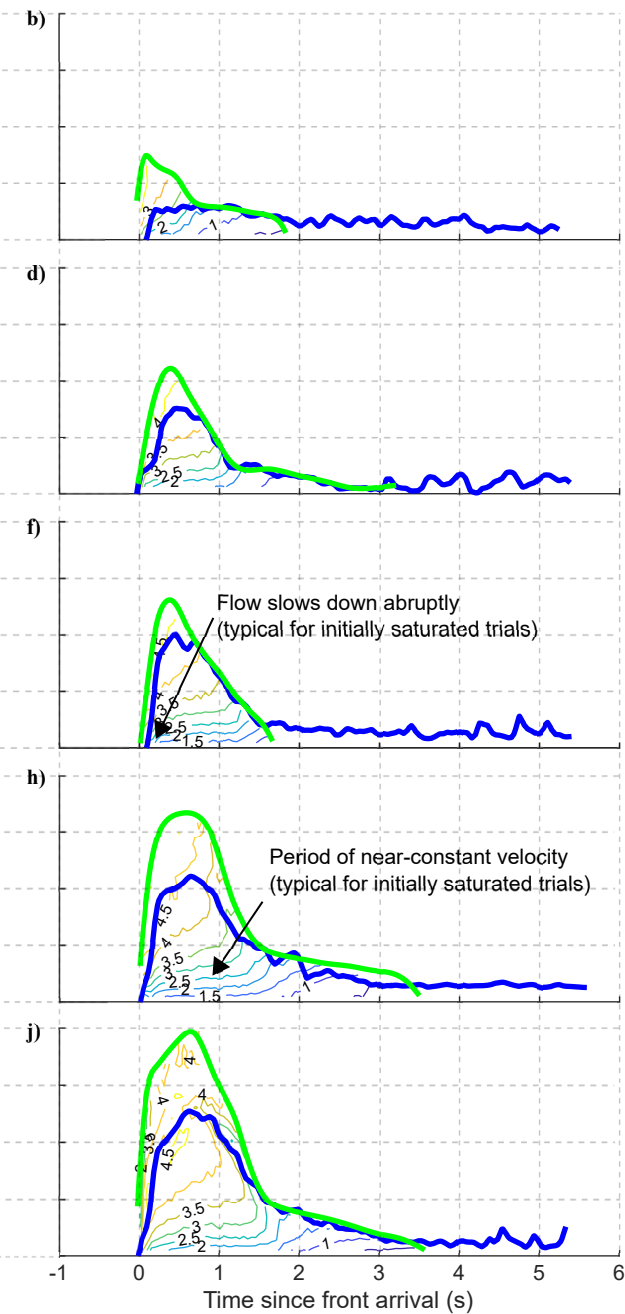
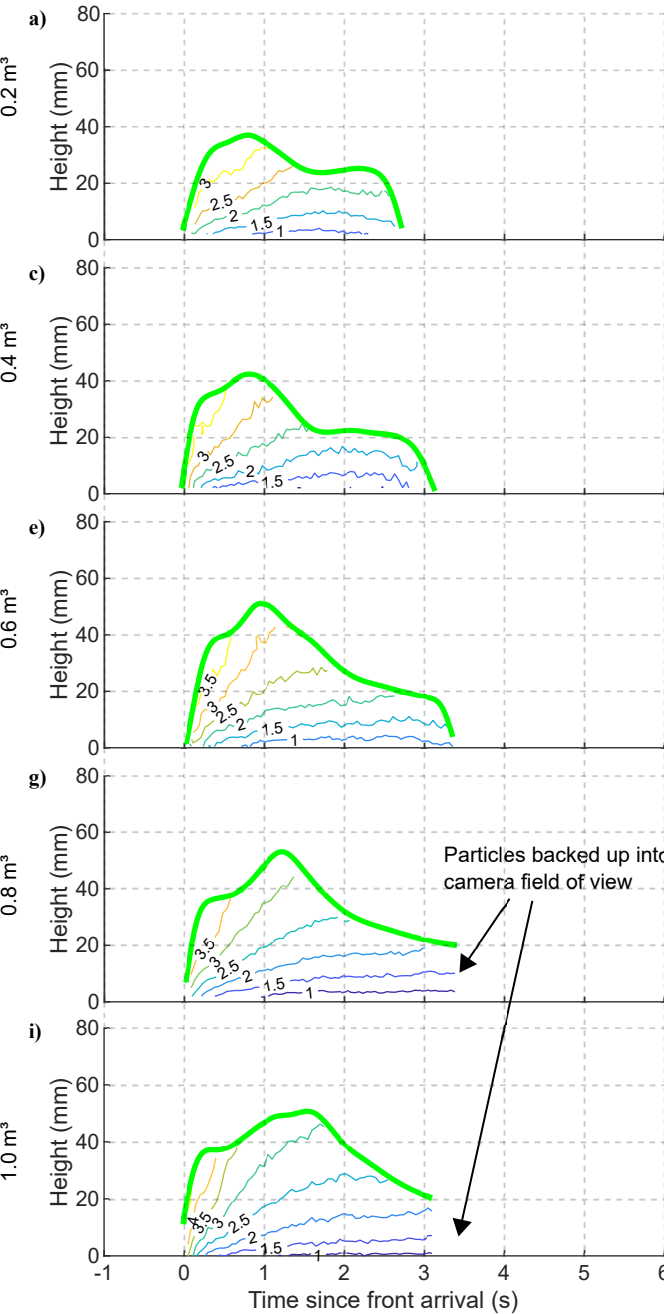


Figure 11.

Dry

Saturated



Contour lines represent streamwise flow velocity as determined by PTV method

Legend

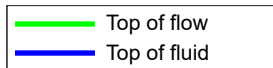
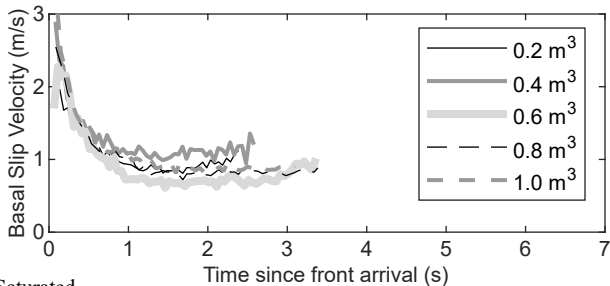


Figure 12.

a) Dry



b) Saturated

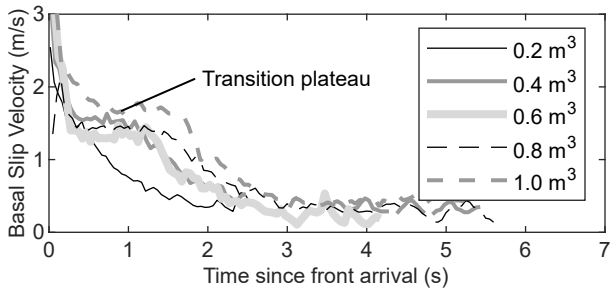
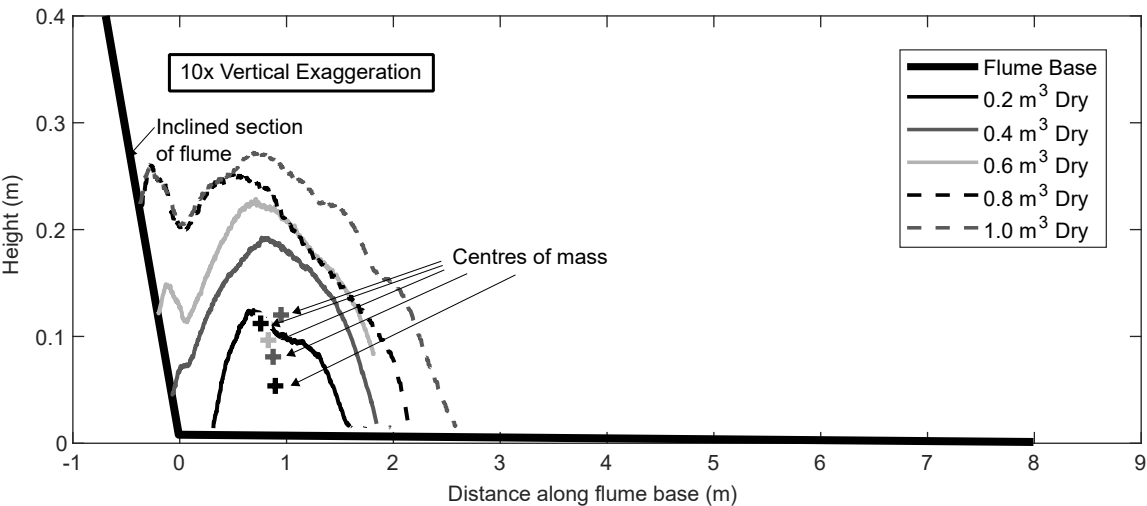


Figure 13.

(a) Dry trials



(b) Initially saturated trials

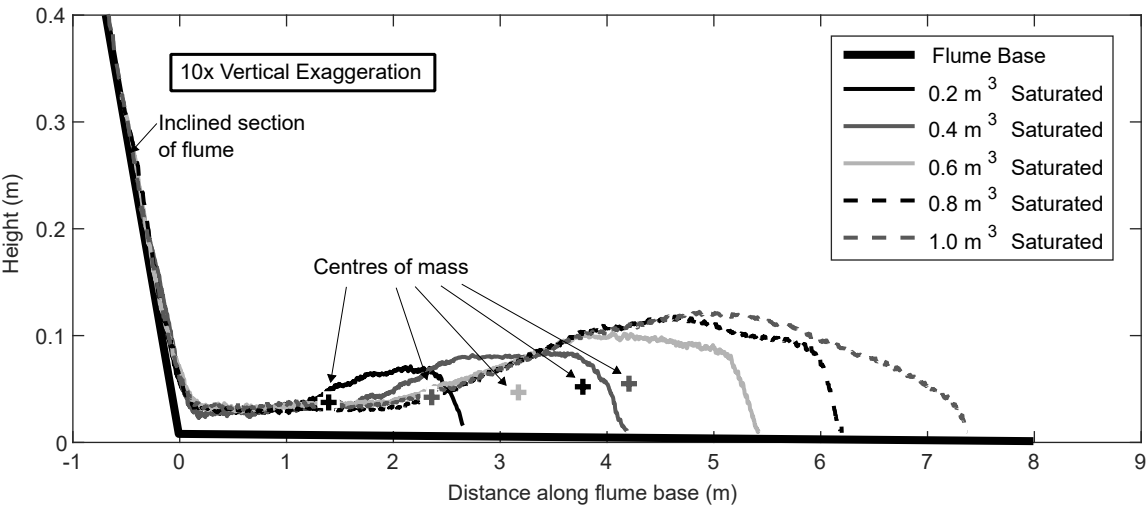


Figure 14.

